



Assessing the utility of visible-to-shortwave infrared reflectance spectroscopy for analysis of soil weathering intensity and paleoclimate reconstruction

Lulu Zhao^a, Hanlie Hong^{a,*}, Jiacheng Liu^b, Qian Fang^a, Yuzeng Yao^c, Wei Tan^b, Ke Yin^a, Chaowen Wang^d, Mi Chen^e, Thomas J. Algeo^{a,f,g,*}

^a School of Earth Sciences, China University of Geosciences, Wuhan 430074, China

^b Key Laboratory of Mineralogy and Metallogeny, Guangzhou Institute of Geochemistry, Chinese Academy of Sciences, Guangzhou 510640, China

^c Department of Geology, Northeastern University, Shenyang, Liaoning 110004, China

^d Gemological Institute, China University of Geosciences, Wuhan 430074, China

^e Hubei Geological Survey, Wuhan 430034, China

^f State Key Laboratory of Geological Processes and Mineral Resources, China University of Geosciences, Wuhan 430074, China

^g Department of Geology, University of Cincinnati, Cincinnati, OH 45221-0013, USA

ARTICLE INFO

Article history:

Received 19 May 2017

Received in revised form 28 June 2017

Accepted 8 July 2017

Available online 14 July 2017

Keywords:

VSWIR

Paleoclimate

Clay minerals

Fe-oxide minerals

CIA

Imaging spectroscopy

ABSTRACT

Visible-to-shortwave infrared reflectance (VSWIR) spectroscopy is a fast and efficient approach for estimation of soil properties. In order to test whether soil weathering intensity can be predicted using reflectance spectra in the VSWIR range (350–2500 nm), and to examine the efficacy of this methodology to supplement or substitute for traditional mineralogical and geochemical techniques of paleoclimate reconstruction, we investigated a Quaternary soil sequence at Shengli in the Sichuan Basin of southwestern China. VSWIR absorption bands can be characterized by geometrical parameters including position (P), depth (D), width (W), asymmetry (AS), and full width at half maximum (F). Our results indicate that spectral features in the visible-to-near-infrared (VNIR; 350–1000 nm) range can be interpreted in terms of the presence and/or concentration of individual Fe-oxide phases. Spectrally detected water is mostly bound in clay minerals, and this single dominant water source facilitates interpretation of shortwave infrared (SWIR; 1000–2500 nm) parameters. Soil spectral parameters were compared with the Fe-oxide mineralogy, major element composition, and clay mineralogy of soil samples obtained from conventional laboratory analyses. Strong correlations are found between VNIR parameters and Fe-oxide mineralogy, with D_{900} serving as the best proxy for total ferric iron concentration. P_{900} and D_{700}/D_{500} exhibit similar variation trends and relationships to the hematite/(hematite + goethite) $[H/(H + G)]$ ratio of soil samples, confirming their value as monsoonal weathering intensity proxies. Lower values of P_{900} and D_{700}/D_{500} indicate warmer and seasonally drier pedoenvironments, reflecting a stronger East Asian summer monsoon. The utility of some SWIR parameters for assessment of weathering intensity declines in inhomogeneous soils (e.g., those having vermiform structure). Thus, spectral evaluation of weathering intensity is most effective in soils that are relatively homogeneous, for which weathering degree is highly correlated to AS_{2200} , D_{2200}/D_{1900} , and AS_{1400} . The utility of these spectral proxies depends mainly on the mineral composition of soils and the application type (i.e., laboratory versus field studies). The application of VSWIR in the field (e.g., imaging spectroscopy, or IS) shows promise for rapid, in-situ mapping of weathering intensity, thus providing a convenient approach to paleoclimate reconstruction in remote and inaccessible regions.

© 2017 Elsevier B.V. All rights reserved.

* Corresponding authors at: School of Earth Sciences, China University of Geosciences, Wuhan 430074, China.

E-mail addresses: honghl8311@aliyun.com (H. Hong), Thomas.Algeo@uc.edu (T.J. Algeo).

1. Introduction

Weathering results in geochemical fractionations in Earth's (near-)surface environment through redistribution of elements between primary and secondary minerals in the process of formation of soils and sediments (Banfield et al., 1999). Exposure of minerals to oxygen initiates chemical and physical reactions, shaping the compositions of the lithosphere, hydrosphere, and atmosphere through

geological time (Lee et al., 2008). Mineral weathering also directly impacts humans, affecting agriculture, water quality, architectural stability, and landscape evolution (White, 2008; Gislason et al., 2009; Dixon et al., 2016; Oh and Shin, 2016). Therefore, assessment of factors controlling weathering is essential for an improved understanding of processes in the Earth's Critical Zone, i.e., the interface of the geologic, atmospheric, and hydrologic systems, in which soil, atmospheric gases, and meteoric water interact (Anderson et al., 2007; Brantley et al., 2007). The Critical Zone is regarded as the dynamic living skin of the Earth, extending from the top of the vegetation canopy downward through the soil and into the upper crust to the level of fresh bedrock and minimal groundwater penetration (Chorover et al., 2007).

Progressive weathering is associated with increased development of secondary minerals such as hydroxyl-bearing clays (e.g., kaolinite and illite) and Fe-oxide minerals (e.g., hematite and goethite), as well as decreased concentrations of mobile cations (e.g., Ca, Na, and K) as a consequence of soil leaching and pedogenesis (Varga et al., 2011; Clift et al., 2014). The nature of soil materials is directly related to the environmental and climatic conditions that prevailed during pedogenesis (Sheldon and Tabor, 2009; Lü et al., 2016; Fang et al., 2017b). Some soil properties determined via laboratory analyses have been identified as proxies for the intensity of pedogenic weathering (Xiong et al., 2010; Újvári et al., 2014; Hong et al., 2016; Mohanty et al., 2016).

Red earth sediments (RESs) in southern China are regarded as valuable archives for evaluating variations in weathering and erosion during the Quaternary (Hong et al., 2010; Lu et al., 2015; Zhao et al., 2017). They cover wide areas of East Asian and can provide a high-resolution record of variations in global climatic conditions and Asian monsoon intensity during the Quaternary (Hu et al., 2010; Wang and Yang, 2013; Fang et al., 2017b). For this purpose, several weathering proxy indices have been proposed, including geochemical proxies such as chemical index of alteration (CIA) and Rb/Sr ratio, clay mineralogy, Fe-oxide mineralogy, magnetic susceptibility, grain size distributions, and biomarkers (Zhang et al., 2009; Hong et al., 2010, 2013, 2016; Hu et al., 2009, 2010; Wang et al., 2013; Lu et al., 2015; Zhao et al., 2017). Most of these proxies are based on conventional laboratory methods that are time consuming and/or expensive, and some chemical extraction procedures can change the equilibrium between solid and solution phases of soils, thus complicating their interpretation (Islam et al., 2003; Summers et al., 2011; Viscarra Rossel et al., 2016). Moreover, development of new weathering proxies is challenging because each proxy needs to be proven as synchronous with weathering events and independent of other indicators (Dufrechou et al., 2015).

In the past decade, reflectance spectroscopy has gained increasing attention for in-situ analysis of soil properties (Viscarra Rossel et al., 2006; Nocita et al., 2015; Adeline et al., 2017). Reflectance spectroscopy is a fast, cost-efficient, and nondestructive method that can be used to predict various soil properties such as pH, moisture, bioactivity, cation exchange capacity, and soil composition (including contents of organic carbon, exchangeable magnesium and calcium, total nitrogen, and carbonate) (Soriano-Disla et al., 2014; Viscarra Rossel et al., 2016). The spectra of diagnostic weathering products such as clay minerals and Fe-oxides lie within the visible to shortwave infrared range (VSWIR; 350–2500 nm) and, therefore, can be used to derive significant information about soil properties (Murphy and Monteiro, 2013; Dufrechou et al., 2015). A few studies have applied VSWIR reflectance spectroscopy to estimation of weathering intensity at a regional scale. For example, it was used to assess the weathering of granite monuments in South Korea by Hyun and Park (2011), to map mineral distributions that provided insights into weathering, erosional and depositional processes in Australia by Cudahy et al. (2016), and to reconstruct climate conditions from lake deposits in Indonesia by Timothy et al. (2017). However, whereas earlier studies have been focused on the spectral information yielded by granites, surface soils, and lake sediments, applications of VSWIR spectroscopy to Quaternary soil sequences and detailed comparison of results with conventional laboratory methods have been limited.

Here, we present a systematic study to determine the extent to which VSWIR reflectance spectra can be applied to evaluation of weathering signals preserved in RES soil deposits. The objectives of this paper are (1) to determine the spectral properties of pedogenic weathering products (i.e., Fe-oxides and clay minerals) in Quaternary RESs of East Asia; (2) to compare the VSWIR spectral parameters of soils with the mineralogical and chemical composition of soil samples as determined using standard techniques, including diffuse reflectance spectroscopy (DRS), X-ray diffraction (XRD) and X-ray fluorescence (XRF); and (3) to discuss the utility of VSWIR spectral parameters for paleoclimate reconstruction and remote sensing as well as limitations thereon.

2. Weathering intensity proxies in soils

Pedogenic weathering is influenced by multiple factors including parent material, time, topography, organisms, and climate (Brady and Weil, 2000; Stockmann et al., 2011). Climate variation (especially precipitation and temperature) plays a major role, although all factors are generally interconnected (Jahn et al., 2001; Anderson et al., 2004; Brantley et al., 2007). Pedogenic properties such as elemental composition, mineralogical composition, and grain size distribution change as weathering proceeds but ultimately trend toward an equilibrium (Sun et al., 2016; Zheng et al., 2016). With greater weathering, mobile and soluble elements (e.g., Na, K, and Ba) are leached from soils, and stable residual elements (e.g., Al and Ti) are enriched (Nesbitt and Young, 1982). Various indices based on elemental ratios have been utilized to estimate the degree of chemical weathering of a soil (Price and Velbel, 2003; Ceryan et al., 2008; Buggle et al., 2011). Furthermore, secondary products such as clay minerals and Fe-oxides form during pedogenesis, so their concentrations and ratios also can provide information about weathering intensity and past climate variability (Sheldon and Tabor, 2009; Wang and Yang, 2013; Clift et al., 2014; Wan et al., 2015). Other soil proxies that can serve as paleoclimate indicators, e.g., $\delta^{13}\text{C}$ and $\delta^{18}\text{O}$ in soil carbonate (Han et al., 1997; Dettman et al., 2003; Sheng et al., 2008), bulk-rock mineralogy in loess-paleosol sequences (Eberl and Smith, 2009; Jeong et al., 2011), and grain morphology (Chen et al., 2010; Lu et al., 2015), will not be considered in this study.

2.1. Proxies based on elemental ratios

The degree of chemical leaching in soils can be quantified by elemental ratios, which are classified as either “Na-type” or “Sr-type” indices (Table 1; Buggle et al., 2011). Na-type indices are calculated as major-element ratios, using Na as the main mobile element and Al as the immobile counterpart. The chemical index of alteration (CIA) was designed to interpret the alteration extent of feldspars and has been widely used in numerous soil studies (e.g., Buggle et al., 2011; Wang et al., 2013; Li et al., 2016). The chemical index of weathering (CIW) and plagioclase index of alteration (PIA) are modifications of CIA that eliminate K, which can exhibit inconsistent behavior during weathering (Price and Velbel, 2003). The chemical proxy of alteration (CPA) removes all potential biases by factoring out both K and Ca, and it is considered as the most promising weathering index for the loess-paleosol sequences in northern China (Buggle et al., 2011).

On the other hand, Sr-type indices are based on trace-element ratios such as Ba/Sr and Rb/Sr. Sr substitutes for Ca in minerals and exhibits a similar behavior to Ca in weathering, whereas Ba and Rb are generally adsorbed by clay minerals after release from weathered primary minerals and, thus, tend to show little depletion in soils. Consequently, in Sr-type indices, Sr represents the mobile component and Ba and Rb the immobile counterparts (Dasch, 1969; McLennan, 1993). Because precipitation of secondary carbonate can lead to misleadingly low Rb/Sr and Ba/Sr ratios, it is recommended that use of Sr-type weathering indices be restricted to carbonate-free materials, for which silicate weathering intensity can be accurately estimated (Buggle et al., 2011).

Table 1
Overview of several commonly used chemical weathering indices.

Chemical weathering indices		Formula	Reference
Na-type	Chemical index of alteration (CIA)	$\left(\frac{\text{Al}_2\text{O}_3}{\text{Al}_2\text{O}_3 + \text{Na}_2\text{O} + \text{CaO} + \text{K}_2\text{O}} \right) * 100$	Nesbitt and Young (1982)
	Chemical index of weathering (CIW)	$\left(\frac{\text{Al}_2\text{O}_3}{\text{Al}_2\text{O}_3 + \text{Na}_2\text{O} + \text{CaO}^*} \right) * 100$	Sheldon et al. (2002)
	Plagioclase index of alteration (PIA)	$\left(\frac{\text{Al}_2\text{O}_3 - \text{K}_2\text{O}}{\text{Al}_2\text{O}_3 + \text{Na}_2\text{O} + \text{CaO}^* - \text{K}_2\text{O}} \right) * 100$	Fedo et al. (1995)
	Chemical proxy of alteration (CPA)	$\left(\frac{\text{Al}_2\text{O}_3}{\text{Al}_2\text{O}_3 + \text{Na}_2\text{O}} \right) * 100$	Cullers (2000)
Sr-type	Ba/Sr	Ba/Sr	Dasch (1969)
	Rb/Sr	Rb/Sr	

All major oxides are expressed in molar proportions and CaO^* represents the content of CaO in silicate-bearing minerals.

The Sr-type indices have gained growing acceptance as weathering proxies during the last two decades (Chen et al., 1999; He et al., 2013; Hošek et al., 2015).

2.2. Proxies related to pedogenic mineral formation and/or transformation

Clay minerals and Fe-oxides can form from solid-state transformations or precipitate from soil solutions during pedogenesis (Wilson, 2004; Huang et al., 2011; Viscarra Rossel, 2011). Their nature is strongly affected by water variability and temperature in soils, which are related to weathering intensity (Nesbitt et al., 1997; Terhorst et al., 2012; Wang and Yang, 2013). Consequently, the composition and abundance of clay minerals and Fe-oxides in soils have been used frequently as indicators of weathering intensity and climate regime (Shaw et al., 2010; Hong et al., 2016; Zhao et al., 2017). In the present study, clay and Fe-oxide mineralogy will be compared with VSWIR reflectance spectral features to test whether the latter can be used as proxies for weathering intensity in the study region.

Pedogenic clay-mineral assemblages are strongly influenced by climate. As climate conditions shift from cool and dry to warm and moist, clay-mineral production follows the sequence illite, chlorite → vermiculite → smectite → kaolinite (Sheldon and Tabor, 2009). Illite is widely present in source rocks undergoing weathering, and it is relatively resistant to alteration during weathering (Chamley, 1989). The neogenesis of illite and chlorite is indicative of low-intensity weathering, typical of cool to temperate conditions (Liu et al., 2010; Wang and Yang, 2013). Smectite, a metastable precursor of kaolinite, is typically an in-situ product of medium-intensity weathering, forming in poorly drained regions (Huang et al., 2011; Varga et al., 2011; Újvári et al., 2014). Kaolinite is the end-product of high-intensity weathering, during which all cations other than Al and Si have been leached out of the soil (Chamley, 1989; Zhao et al., 2017). It is typical of warm, wet conditions, such as in the subtropical monsoon belt (Thiry, 2000; Hong et al., 2013).

Neoformed Fe-oxides (e.g., maghemite, magnetite, hematite, and goethite) in soils are also useful paleoclimate proxies. Increases in magnetic susceptibility (χ) in soils are typically due to the presence of pedogenic maghemite and magnetite (Maher, 1998). Strong linkage exists between magnetic susceptibility variations in Chinese Quaternary loess-paleosol sequences and the marine O-isotope record, indicating that magnetic susceptibility is an accurate record of terrestrial paleoclimate changes (Deng et al., 2004; Torrent et al., 2007; Hu et al., 2015). The proportion of hematite and goethite in soils, commonly given as the hematite/(hematite + goethite) ratio $[H/(H + G)]$, is strongly related to temperature and rainfall seasonality (Cornell and Schwertmann, 2003; Buggle et al., 2014). Hematite production is favored in warm and seasonally wet settings with high MAP, whereas goethite is favored in cooler and drier settings (Torrent et al., 2007; Zhao et al., 2017).

3. Materials and methods

3.1. Regional setting

The study area is situated in the Sichuan Basin of southwestern China (450–650 masl, or meters above sea level), which is surrounded by the Qinling Mountains (2000–3000 masl) to the north, the Chuanxi Plateau (2000–4500 masl) to the west, and the Yunnan-Guizhou Plateau (~2000 masl) to the south (Fig. 1; Yang et al., 2010). The Yangtze River and several of its large tributaries (e.g., the Jialingjiang, Tuojiang, and Minjiang rivers) flow through the basin, forming alluvial plains. The Sichuan Basin belongs to subtropical monsoonal climate zone, which is characterized by large seasonal variations in air temperature, wind direction, and rainfall, with >80% of precipitation during the period from May to September (Han et al., 2010). The environment and climate of the Sichuan Basin are mainly influenced by the East Asian and the Indian monsoon systems (Fig. 1; An, 2000; Zhao et al., 2017). During summer, the basin is dominated by the East Asian Summer Monsoon (EASM) and Indian Summer Monsoon (ISM), which advect warm, humid airmasses from the Pacific and Indian oceans, respectively, and during winter, the westerly Jetstream is dominant because cold airmasses of the East Asian Winter Monsoon (EAWM) are mostly blocked by the Qinling Mountains and the Tibetan Plateau.

3.2. Study section and soil samples

The Shengli section (30°31'N, 103°54'E) is located in the southwestern part of the Sichuan Basin in Sichuan Province, southwestern China. This area has a monsoon-influenced subtropical climate with mean annual temperature (MAT) and mean annual precipitation (MAP) of 16.5 °C and 1150 mm, respectively. The section is ~15 m thick and consists of four stratigraphic units (from bottom to top): Unit 1 (12.0–15.0 m): sandy clay; Unit 2 (3.5–12.0 m): silty clay; Unit 3 (1.0–3.5 m): clay loam; and Unit 4 (0–1.0 m): loam (see Zhao et al., 2017, their Fig. 2, for section illustration). A total of 76 samples was collected in outcrop at a stratigraphic spacing of 20 cm, and the weight of each sample was ~1 kg. All the samples were trimmed to remove visible veins and weathered surfaces.

Samples between 3.5 and 14 m exhibit vermiform clay features (VC samples; $n = 52$). The vermiform clay is generally composed of white net-like veins or spots and red matrix. The white veins/spots are produced by Fe leaching during intense weathering, whereas the red matrix retains a high Fe-oxide content (Rosolen et al., 2002; Hong et al., 2010). The vermiform soils are developed in seasonally wet-dry climates, in which microorganisms and groundwater table fluctuations promote localized Fe leaching (Hong et al., 2010, 2016). The samples at 0–3.5 m and 14–15 m do not exhibit any vermiform character (non-VC samples; $n = 24$). The most significant compositional difference between the VC and non-VC samples is in total clay-mineral content. The VC samples have

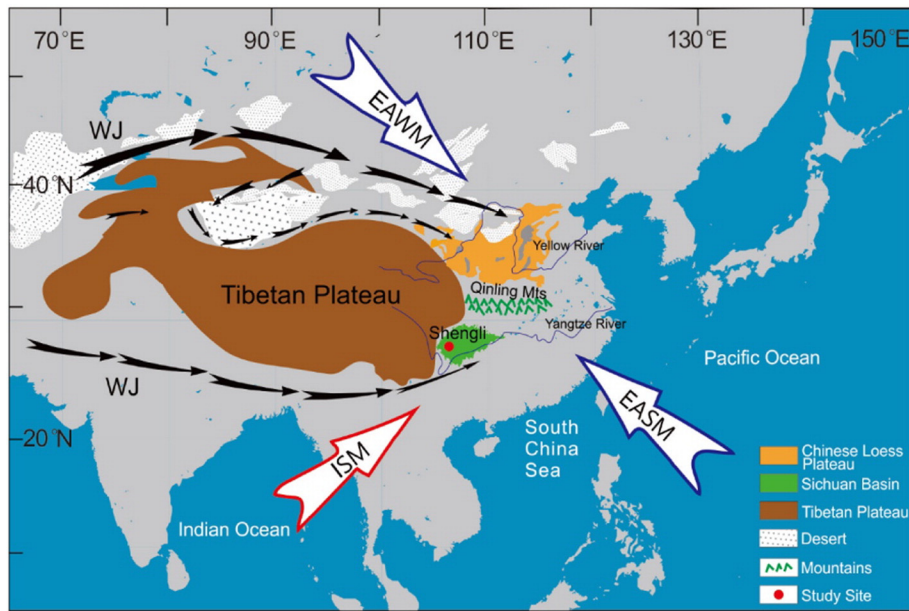


Fig. 1. Map showing major monsoon regimes in East Asia with the location of the Shengli section. ISM—Indian summer monsoon, EASM—East Asian summer monsoon, EAWM—East Asian winter monsoon, WJ—Westerly jet. (Modified from Gong et al., 2015).

total clay contents ranging from 36.0% to 47.8% (mean 42.2%), whereas the non-VC samples have lower values ranging from 19.9% to 41.7% (mean 34.2%).

Bulk samples were dried and ground to ~200 mesh size before VSWIR analysis. Age constraints, clay mineralogy, Fe-oxide content, and other geochemical data for the Shengli section were reported by Zhao et al. (2017). The total clay content of each sample was estimated as:

$$\text{Total clay content (\%)} = \text{Al}_{\text{measured}} \times 100/\kappa \quad (1)$$

where the constant κ represents the average concentration of Al in the clay mineral assemblage. We adopted a fixed value of 12.5 for κ (based

on the analysis of Algeo et al., 2007) that, despite some uncertainty in the resulting absolute estimates of total clay content, does not affect the secular trends shown in vertical profile.

3.3. Soil spectral measurements

3.3.1. Principles of reflectance spectroscopy

Reflectance spectroscopy is the study of light as a function of wavelength that has been emitted, reflected, or scattered from a solid, liquid, or gas. It is based on how radiation in the electromagnetic spectrum interacts with a surface and is reflected back to a detector such as a

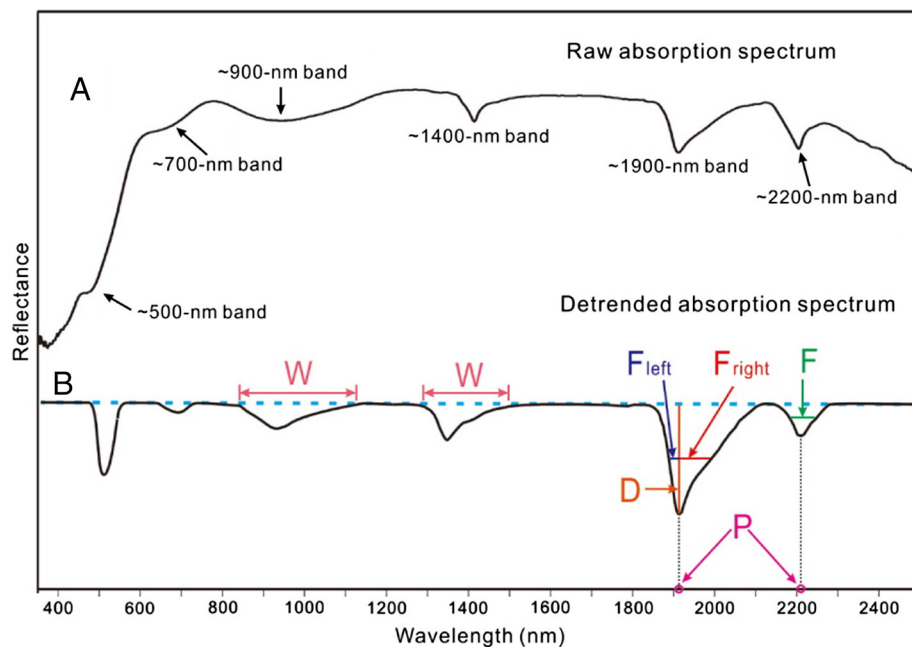


Fig. 2. Examples of (A) a raw absorption spectrum for a silty clay sample (at ~11 m), and (B) a detrended absorption spectrum, showing geometrical parameters used to characterize absorption bands, i.e., position (P; purple circles), depth (D; orange line), width (W; pink segment), and full width at half maximum (F; green line). Asymmetry is quantified as the ratio between the left width at half maximum (F_{left} ; blue line) and the right width at half maximum (F_{right} ; red line). Note that the depth are values relative to the height of standard BaSO_4 spectra.

spectrometer (Clark, 1999). Minerals with spectrally active components exhibit unique absorption features, and variations in crystalline structure and mineralogic composition can cause shifts in the position and shape of absorption bands (Bo et al., 2010; Summers et al., 2011; Fang et al., 2017a). Moreover, reflectance spectroscopy is more sensitive to minerals with strong absorption bands, such as clay minerals and Fe-oxides (Zheng et al., 2016). However, the VSWIR region is insensitive to the presence of some minerals in soils, such as quartz and feldspar

(Mulder et al., 2013). Spectral absorption bands reflect absorption of energy quanta due to displacement of electrons between different orbitals of a given element (Farmer and Russell, 1964; Burns, 1993). Because diagnostic absorption features of Fe-oxides are primarily located in the visible/near-infrared region (VNIR, 350–1000 nm) and those of clay minerals in the shortwave infrared region (SWIR, 1000–2500 nm), this study is concerned with the entire VSWIR spectrum (350–2500 nm).

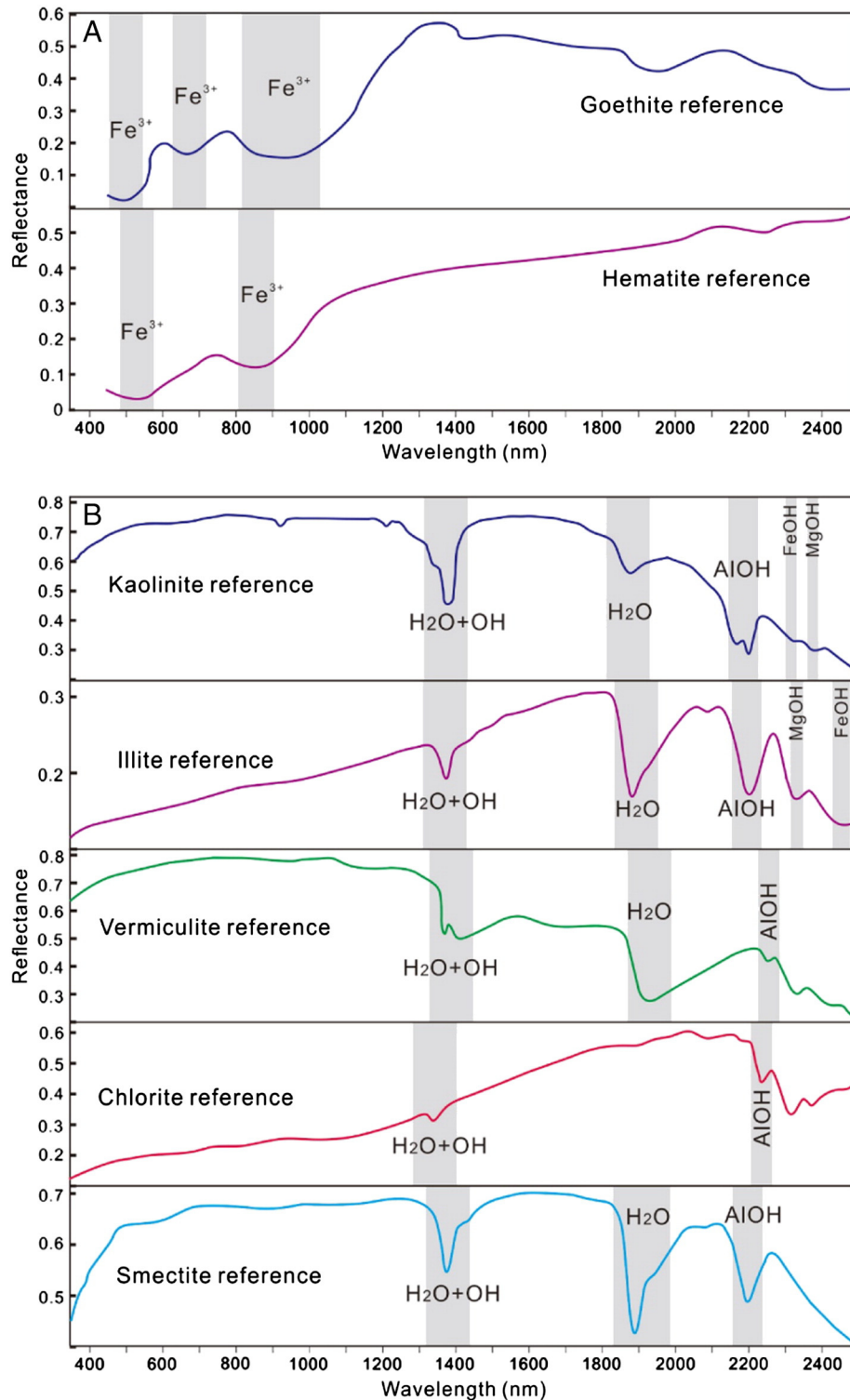


Fig. 3. Reference spectra for (A) Fe-oxides and (B) clay minerals (Clark et al., 2007). Note that the absorption features of Fe-oxides are mainly in the VNIR range and those of clay minerals mainly in the SWIR range.

3.3.2. VSWIR spectroscopy

All samples were air dried in an oven at 65 °C for 48 h and then passed through a 1-mm sieve, but no further treatment prior to spectral measurement was carried out. The samples were spectrally measured using an Analytical Spectral Devices (ASD) FieldSpec-3 spectrometer with a spectral resolution of ~8 nm and a sampling interval of 1 nm. VSWIR spectra of the soil samples were measured with an external light source and the bare ASD fiber optic cable. The instrument has a range from 350 to 2500 nm, covering the entire VSWIR spectrum. Three reflectance spectra were obtained for each sample, and each spectral reading was based on duplicate measurements in order to achieve a robust output. In order to maintain stable analytical conditions, the instrument was recalibrated every ~20 min during use. The collected spectra were processed with the Spectral Geologist (TSG™) software, and the peak parameters were calculated from hull-removed spectra using the hull quotient baseline correction (Fig. 2; Clark and Roush, 1984; Dufrechou et al., 2015).

3.3.3. Spectral parameters

VSWIR absorption bands can be described by geometrical parameters such as position (P), depth (D), width (W), full width at half maximum (FWHM, abbreviated to 'F'), and asymmetry (AS) (Fig. 2; van der Meer, 2004; Dufrechou et al., 2015). These geometrical parameters are illustrated in Fig. 3 and summarized in Table 2. The position (P) is defined as the wavelength corresponding to peak absorption in an absorption band, and it is regarded as the most diagnostic parameter for mineral identification (Dufrechou et al., 2015). The depth (D) corresponds to the difference between the reflectance values of the nadir (i.e., absorption maximum) and those at the shoulders of an absorption band. The width (W) represents the width of an individual spectral band from one shoulder to the other. The full width at half maximum (F) represents the width of the absorption band at half the depth, i.e., mid-way between the background and nadir (i.e., absorption maximum) values. P, W, and F have units of nm, and depth, being relative to the height of a BaSO₄ standard spectrum, is dimensionless. The asymmetry (AS) of the absorption band is calculated from the ratio between the left width at half maximum (F_{left}) and the right width at half maximum (F_{right} ; Dufrechou et al., 2015):

$$AS = \frac{F_{\text{left}}}{F_{\text{right}}} \quad (2)$$

As described by van der Meer (2004), AS = 1.0 indicates a symmetric absorption band, and AS > 1.0 is defined as leftward asymmetry and AS < 1.0 as rightward asymmetry.

3.3.4. Absorption bands in the VNIR region

Absorption in the VNIR region (350–1000 nm) is associated mainly with electronic transitions in unfilled *d*-orbitals of Fe-oxide minerals (Cornell and Schwertmann, 2003; Tappert et al., 2011). Electronic transitions generally yield broad and smooth absorption bands (Fig. 3A). Hematite (α -Fe₂O₃) and goethite (α -FeOOH) exhibit diagnostic spectral features in the VNIR region. The bands are caused by absorption in ferric iron, which induces crystal field transitions at ~465 nm (${}^6A_{1g} \rightarrow {}^4T_{1g}$, 4E_g), ~650 nm (${}^6A_{1g} \rightarrow {}^4T_{2g}$), and ~900 nm (${}^6A_{1g} \rightarrow {}^4T_{1g}$; Fig. 3A; Townsend, 1987). The spectral absorption bands in the VNIR range are positively correlated with the relative concentrations of hematite and goethite in a soil sample (Murphy and Monteiro, 2013).

3.3.5. Absorption bands in the SWIR region

Absorption in the SWIR region (1000–2500 nm) is frequently associated with molecular components (e.g., H₂O, OH—, or CO₃²⁻) common in phyllosilicate and carbonate minerals (Clark et al., 1990; Timothy et al., 2017). The bands produced by vibrational processes are relatively narrow and sharp (Fig. 3B). The excitation of overtones causes the absorption bands of molecular water and OH (hydroxyl) at ~1400 nm and

~1900 nm, respectively (Da Cruz et al., 2015; Zheng et al., 2016). The combination tones of OH[−] bending and stretching vary significantly in the 2000–2500 nm range, depending on the specific octahedral cations (e.g., Al, Fe, Mg) bound to the OH[−] ions. The spectral features of some common clay minerals are given in Table 3. Kaolinite and illite, which are generally shown with warmer and cooler tones, respectively, comprise >80% of clay minerals in RESs of the present study section (Zhao et al., 2017). Kaolinite-group minerals reveal OH[−] radical bands controlled by an Al—OH doublet near 2200 nm (at ~2163 and ~2208 nm) and an OH doublet near 1400 nm (at ~1395 and ~1415 nm). The intensity of the doublets is controlled by the location of the hydroxyl ion in the mineral structure, and structurally well-ordered kaolinite and poorly ordered halloysite reveal well-defined and weak doublets, respectively (Da Cruz et al., 2015). Illite shows relatively symmetric and sharply defined Al—OH spectral bands and overtone bands centered at 2200, 1400, and 1900 nm (Dufrechou et al., 2015). Additionally, the Al—OH band is modified by Fe and Mg Tschermak cation exchange, and therefore kaolinite and illite exhibit weak spectral features in the 2180–2500 nm region (Clark et al., 1990; Duke, 1994).

4. Results

4.1. VSWIR absorption spectra in mineralogically mixed soils

Overlapping absorption bands pose a problem in determining the mineral phases present in an unknown soil deposit, especially when a mixture of minerals with similar absorption spectra are present. For example, many Fe-oxides exhibit overlapping bands in the VNIR range, and many clay minerals exhibit overlapping bands in the SWIR range (Fig. 4). However, this problem is alleviated in soils for which the mineral composition has been previously determined by other methods, which is the case for the Shengli section. As shown by XRD and DRS analyses, the Shengli section is dominated by hematite, goethite, kaolinite, and illite (Zhao et al., 2017).

In the Shengli RESs, the most distinctive and characteristic feature in the VNIR range is crystal field absorption of ferric iron (Fe³⁺) at ~900 nm. However, this absorption band is also shared with goethite and other Fe-oxides (e.g., lepidocrocite, maghemite, and ferrihydrite), so it is necessary to consider secondary absorption peaks at ~500 nm and ~700 nm to accurately characterize Fe-oxide mineralogy. Theoretically, there is barely any absorption at ~700 nm for hematite (Fig. 3A), so the presence or absence of this absorption peak can be used to distinguish goethite from hematite.

The SWIR reflectance spectra of the RESs are characterized by a series of distinct vibrational absorptions related to the presence of phyllosilicates (Fig. 4). The spectra of the samples from the whole section are spectrally dominated by absorption bands of kaolinite and illite, including narrow, sharp bands centered at ~1400, ~1900, and ~2200 nm. The absorption band at ~1400 nm is caused by the first

Table 2

Abbreviations of the VSWIR geometrical parameters used in this study.

VSWIR parameters	Description
D ₅₀₀	Depth of absorption band at ~500 nm
D ₇₀₀	Depth of absorption band at ~700 nm
P ₉₀₀	Position of absorption band at ~900 nm
D ₉₀₀	Depth of absorption band at ~900 nm
D ₁₄₀₀	Depth of absorption band at ~1400 nm
AS ₁₄₀₀	Band asymmetry at ~1400 nm
W ₁₄₀₀	Band width at ~1400 nm
P ₁₉₀₀	Position of absorption band at ~1900 nm
D ₁₉₀₀	Depth of absorption band at ~1900 nm
P ₂₂₀₀	Position of absorption band at ~2200 nm
D ₂₂₀₀	Depth of absorption band at ~2200 nm
F ₂₂₀₀	Band width at half depth at ~1400 nm
AS ₂₂₀₀	Band asymmetry at ~2200 nm
W ₂₂₀₀	Band width at ~2200 nm

Table 3
Diagnostic absorption features of the weathering products in the VSWIR (350–2500 nm) range.

Minerals	Description for diagnostic absorption features	Reference
Hematite	Broader absorption near 500 and 920 nm	Clark et al. (2007)
Goethite	Broader absorption near 500, 700 and 920 nm	
Illite	Narrow absorption at 1400, 1900, and 2200 nm; additional absorption near 2340 nm	
Kaolinite	Doublet absorption near 1400 nm and 2200 nm	Clark et al. (1990)
Vermiculite	Narrow absorption at 1400 and 1900 nm; weak absorption near 2200 and 2300 nm	
Chlorite	Triple absorption features near 2300 nm	
Smectite	Strong and sharp absorption at 1400, 1900, and 2200 nm; weak feature on the right of absorption at 1400 and 1900 nm	

overtone of OH[−] stretching, and the absorption band at ~1900 nm by a combination tone of OH[−] stretching and H—O—H bending in structural/adsorbed H₂O (Clark et al., 1990; Gaffey et al., 1993). The broader absorption band of Al—OH at ~2200 nm and the barely discernable bands in the 2180–2500 nm region are characteristic of both kaolinite and illite. Generally, the bands at 2315 nm and 2385 nm represent the presence of kaolinite, and the bands at 2352 nm and 2445 nm are characteristic of illite. The combination tones of Fe—OH (i.e., absorption at 2315 nm and 2445 nm) and Mg—OH (i.e., absorption at 2352 nm and 2385 nm) are observed in almost all spectra, suggesting partial replacement of octahedral Al by Fe and/or Mg (Clark et al., 1990; Duke, 1994).

The soil samples also exhibit several spectral differences associated with variations in weathering degree of soils. The ~900 nm absorption is greatly subdued with decreasing weathering degree (Fig. 4A). The spectra of illite-rich samples (i.e., loam and clay loam) have relative symmetric absorption peak at ~1900 and ~2200 nm (Fig. 4A–B). Additionally, the spectra of the kaolinite-rich samples (i.e., silty clay and sandy clay) show subtle deflections near 1400 nm and 2200 nm (Fig. 4C–D), which are caused by the OH doublets and Al—OH doublets of kaolinite.

4.2. Comparison of VSWIR spectra with Fe-oxide data

Relationships of Fe-oxide minerals to VSWIR spectral parameters are shown in Table 4 and Figs. 5, 7 and Fig. S1. In general, the selected

spectral parameters produced statistically significant correlations, with absolute correlation coefficients ($|r|$) ranging from 0.48 to 0.83 (Fig. 7 and Fig. S1). Ferric oxides are characterized by large D_{500} values (from 0.13 to 0.45) and small D_{900} values (from 0.04 to 0.17). Ferric oxide abundance (Fe₂O₃ wt%) increased with D_{500} and D_{900} , yielding correlation coefficients (r) of +0.65 and +0.72, respectively ($n = 46$; $p < 0.001$; Fig. 7A and Fig. S1A). Hematite/(hematite + goethite) [H/(H + G)] ratios exhibit significant linear correlations with P_{900} , D_{700}/D_{500} , and D_{500} ($r = -0.83$, -0.81 , and $+0.74$, respectively; $n = 76$; $p < 0.001$; Fig. 7B and Fig. S1B–C). Increasing H/(H + G) ratios shift P_{900} toward shorter wavelengths (from 963 nm to 902 nm). The D_{700}/D_{500} proxy, which is original to the present study, takes into account changes in goethite content and ferric Fe-oxide concentration, and it shows a stronger correlation to H/(H + G) ratio than either the D_{700} or D_{500} parameter individually ($r = -0.60$ and $+0.74$; $n = 76$; $p < 0.001$; Table 4). Theoretically, the D_{700} band is directly influenced by the amount of goethite in soils (Murphy et al., 2014), and the significant correlation between D_{700} and goethite observed in the present study ($r = -0.48$; $n = 76$; $p < 0.001$; Fig. S1D) confirms this relationship.

4.3. Comparison of VSWIR spectra with clay mineral data

Relationships of clay minerals to VSWIR spectral parameters are shown in Table 4 and Figs. 6, 7, and Fig. S1. The correlations between clay minerals and spectral parameters in the SWIR range are generally low, with average $|r|$ of 0.31 for kaolinite and $|r|$ of 0.28 for illite. Because illite strongly covaries with kaolinite ($r = -0.98$; $n = 76$; $p < 0.001$; Table 4), examination of the relationships of just one clay mineral to spectral parameters is sufficient (Fig. 7 and Fig. S1). Kaolinite content exhibits strongly significant relationships with AS_{2200} and F_{2200} ($r = +0.70$ and $+0.60$, respectively; $n = 76$; $p < 0.001$; Fig. 7C and Fig. S1E) but non-significant to weak relationships for the other spectral parameters (i.e., P_{2200} , W_{2200} , and D_{2200} , yielding $r = +0.07$, -0.22 and $+0.35$, respectively; $n = 76$; $p > 0.05$, >0.05 and <0.01 , respectively; Fig. S1F–H). The spectral parameters of the absorption bands at ~1400 nm and ~1900 nm (i.e., D_{2200}/D_{1900} , W_{1400} , AS_{1400} , and P_{1900}) show moderate correlations with kaolinite content ($r = +0.40$, -0.39 , $+0.53$ and -0.42 , respectively; $n = 76$; $p < 0.01$; Fig. 7D and Fig. S1I–K). The absorption bands at ~2200 nm and ~1400 nm are characterized by leftward asymmetry. As the

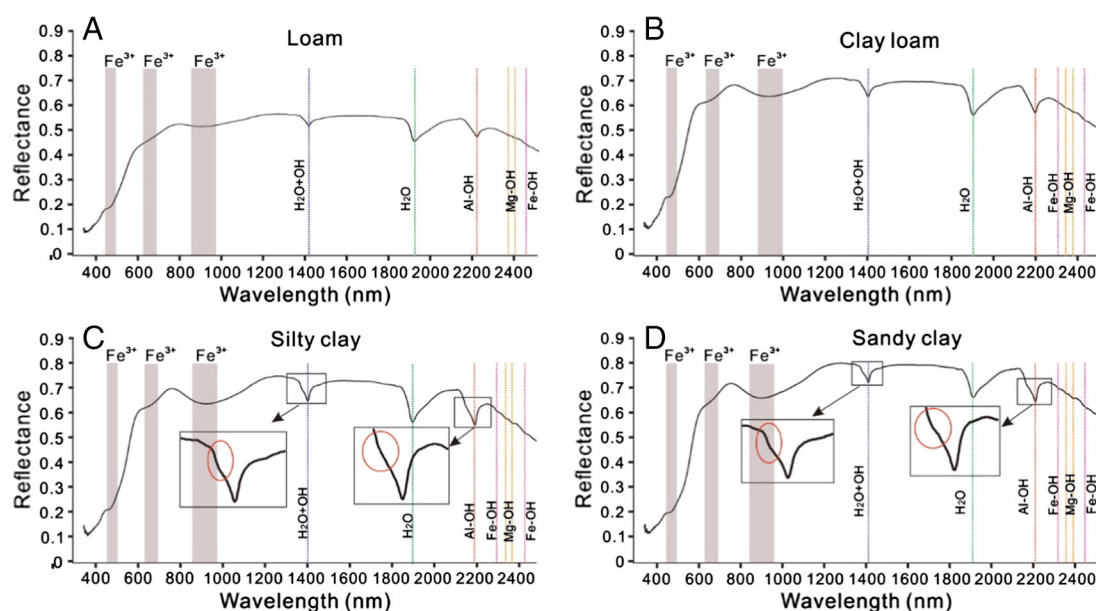


Fig. 4. Representative VSWIR spectra of different lithologies in the Shengli section. Absorption features are shown as shaded fields (at ~500, 700, 900 nm) and dashed lines (at ~1400, 1900, 2200, 2315, 2352, 2385, and 2445 nm).

kaolinite content increases, the degree of leftward asymmetry increases, as seen in shifts of AS_{2200} from 1.30 to 1.53 and AS_{1400} from 1.09 to 1.38 (Fig. 6D, I). The P_{2200} and P_{1900} bands exhibit variation ranges of <3 nm (i.e., 2205.7–2206.8 nm and 1911.3–1913.6 nm, respectively), which are far smaller than the ~60-nm variation range of P_{900} (902.7–963.8 nm), indicating no significant shifts in wavelength positions in the SWIR range (Fig. 6H and Fig. S1K). An increase in kaolinite content of the soil samples is accompanied by a decrease in W_{1400} (from 46.5 to 40.1 nm; Fig. S1I) and W_{2200} (from 54.8 to 52.6 nm; Fig. 6G).

One noteworthy finding is that the samples exhibiting vermiform clay (VC) features (at 3.5–14 m) and those lacking such features (at 0–3.5 m and 14–15 m) exhibit different correlations between spectral parameters and soil composition (Fig. 7 and Fig. S1). Significant correlations are observed between spectral parameters and kaolinite content in the non-VC samples, with $|r|$ ranging from 0.52 to 0.91. All correlations for the non-VC samples are higher than that for all samples as a single group. In contrast, the VC samples yield correlations that are either much weaker than or opposite in those of all samples as a group. For example, AS_{2200} values exhibit much stronger correlations with kaolinite content in the non-VC samples ($r = +0.85$; $n = 24$; $p < 0.001$) than in the VC samples ($r = 0$; $n = 52$; $p > 0.1$) (Fig. 7C). As another example, D_{2200}/D_{1900} values and kaolinite content exhibit a strong positive correlation in the non-VC samples ($r = +0.91$; $n = 24$; $p < 0.001$), a positive correlation in all samples as a group ($r = +0.40$; $n = 76$; $p < 0.01$), and a weak negative correlation in the VC samples ($r = -0.37$; $n = 52$; $p < 0.02$) (Fig. 7D).

4.4. Comparison of VSWIR spectra with geochemical weathering proxies

Relationships of geochemical weathering proxies (e.g., CIA) to VSWIR spectral parameters are shown in Table 4 and Figs. 5–7, and Fig. S1. In general, the selected spectral parameters in both the VNIR (D_{900} and W_{900}) and the SWIR ranges (D_{2200} , D_{2200}/D_{1900} , AS_{1400} and D_{1400}) produced good correlations with CIA, yielding r of +0.70, +0.58, +0.70, +0.69, and +0.62, respectively ($n = 46$; $p < 0.001$; Fig. S1L–P). Furthermore, the asymmetries of the absorption bands at ~2200 nm (AS_{2200}) and ~1400 nm (AS_{1400}) significantly correlate with CIA ($r = +0.79$ and +0.80, respectively; $n = 46$; $p < 0.001$; Fig. 7E–F).

VC and non-VC samples show distinctly different correlations between geochemical proxies and spectral parameters. Whereas Al_2O_3 concentrations show moderate or no significant relationship to AS_{2200} and D_{2200} for all samples as a group ($r = -0.34$ and +0.16, respectively; $n = 46$; $p < 0.05$ and > 0.1 , respectively), these parameters are significantly inversely correlated for non-VC samples ($r = -0.99$ and -0.75 , respectively; $n = 12$; $p < 0.001$; Fig. S1Q–R). In the VC samples, the relationship between Al_2O_3 and D_{2200} is significant ($r = +0.70$; $n = 34$; $p < 0.001$; Fig. S1R), whereas no significant correlations are found between Al_2O_3 and AS_{2200} ($r = -0.21$; $n = 34$; $p > 0.1$; Fig. S1Q). Excellent positive correlations are also observed between CIA and spectral parameters for non-VC samples, with r ranging from +0.79 to +0.95 ($n = 12$; $p < 0.001$; Fig. 7E–F and Fig. S1L–P). In contrast, VC samples exhibit weak or non-significant correlations of CIA and spectral parameters ($0.08 < |r| < 0.63$; $n = 34$; $p < 0.05$ or > 0.1 ; Fig. 7E–F and Fig. S1L–P).

5. Discussion

5.1. Relationships of VSWIR spectral parameters

Absorption behavior in the VNIR range is affected by various sediment properties including Fe-oxide mineral content, aluminum substitution, and grain size (Cudahy and Ramanaidou, 1997). The position and shape of the VNIR absorption bands at ~500, ~700, and ~900 nm are mainly affected by the composition and content of Fe-oxides (Zheng et al., 2016). Whereas aluminum-free hematite and goethite show absorption bands centered at 860 and 915 nm, respectively (Fig.

Table 4
Correlation matrix of r values for spectral parameters and other weathering proxies from the Shengli section.

	CIA	K	I	H/(H + G)	P ₅₀₀	D ₅₀₀	D ₇₀₀	P ₉₀₀	D ₉₀₀	W ₉₀₀	P ₁₄₀₀	D ₁₄₀₀	F ₁₄₀₀	AS ₁₄₀₀	W ₁₄₀₀	P ₁₉₀₀	D ₁₉₀₀	F ₁₉₀₀	P ₂₂₀₀	D ₂₂₀₀	F ₂₂₀₀	AS ₂₂₀₀	W ₂₂₀₀
CIA	1	0.74	-0.73	0.65	0.34	0.51	0.23	-0.22	0.71	0.58	0.26	0.61	-0.12	0.80	-0.44	-0.64	0.37	-0.29	0.49	0.70	0.62	0.79	-0.53
K		1	-0.98	0.51	0.22	0.35	0.05	-0.13	0.48	0.49	0.03	0.24	-0.06	0.53	-0.39	-0.42	0.09	-0.28	0.07	0.35	0.60	0.76	-0.22
I			1	-0.52	-0.19	-0.31	-0.02	0.10	-0.44	-0.17	-0.03	-0.22	0.05	-0.53	0.37	0.38	-0.08	0.27	0.05	-0.32	-0.63	0.22	0.22
H/(H + G)				1	0.39	0.74	-0.60	-0.83	0.37	0.06	0.17	0.45	-0.31	0.66	-0.56	-0.44	0.47	-0.35	0.37	0.61	0.35	0.48	-0.60
P ₅₀₀					1	0.42	-0.06	-0.35	0.45	-0.05	0.35	0.35	-0.11	0.36	-0.34	-0.06	0.03	-0.06	0.34	0.41	0.06	0.46	-0.40
D ₅₀₀						1	-0.22	-0.73	0.72	0.15	0.02	0.61	-0.13	0.44	-0.32	-0.51	0.36	-0.19	0.25	0.69	0.29	0.41	-0.50
D ₇₀₀							1	0.73	0.45	0.58	-0.08	0.22	0.35	-0.05	0.45	-0.09	0.41	0.27	-0.03	0.08	0.10	0.11	0.18
P ₉₀₀								1	-0.08	-0.22	-0.22	-0.24	0.42	-0.46	0.57	0.22	0.08	0.32	-0.38	-0.41	0.05	-0.25	0.55
D ₉₀₀									1	0.62	0.04	0.81	0.04	0.39	-0.04	0.45	0.73	0.12	0.15	0.82	0.64	0.60	0.33
W ₉₀₀										1	0.01	0.37	0.30	0.27	0.15	-0.36	0.43	0.13	-0.04	0.31	0.65	0.38	-0.02
P ₁₄₀₀											1	0.13	-0.32	0.61	-0.14	0.37	-0.01	0.21	0.70	0.16	-0.09	0.37	0.42
D ₁₄₀₀												1	0.44	0.47	0.12	0.44	0.94	0.19	0.16	0.96	0.52	0.47	0.31
F ₁₄₀₀													1	-0.50	0.72	-0.03	0.71	0.58	-0.61	0.25	0.47	-0.10	0.50
AS ₁₄₀₀														1	-0.65	-0.25	-0.06	-0.37	0.70	0.46	0.33	0.70	-0.48
W ₁₄₀₀															1	0.43	0.53	0.84	-0.52	-0.14	0.03	-0.43	0.42
P ₁₉₀₀																1	-0.23	0.62	-0.10	-0.51	-0.35	-0.36	0.07
D ₁₉₀₀																	1	0.50	-0.14	0.75	0.48	0.24	-0.06
F ₁₉₀₀																		1	0.50	-0.34	0	0.08	-0.23
P ₂₂₀₀																			1	1	-0.30	0.42	-0.69
D ₂₂₀₀																				1	0.52	0.59	-0.42
F ₂₂₀₀																					1	0.53	0.03
AS ₂₂₀₀																						1	-0.49
W ₂₂₀₀																							1

Note: Bold text indicates statistically significant r values ($p < 0.05$).

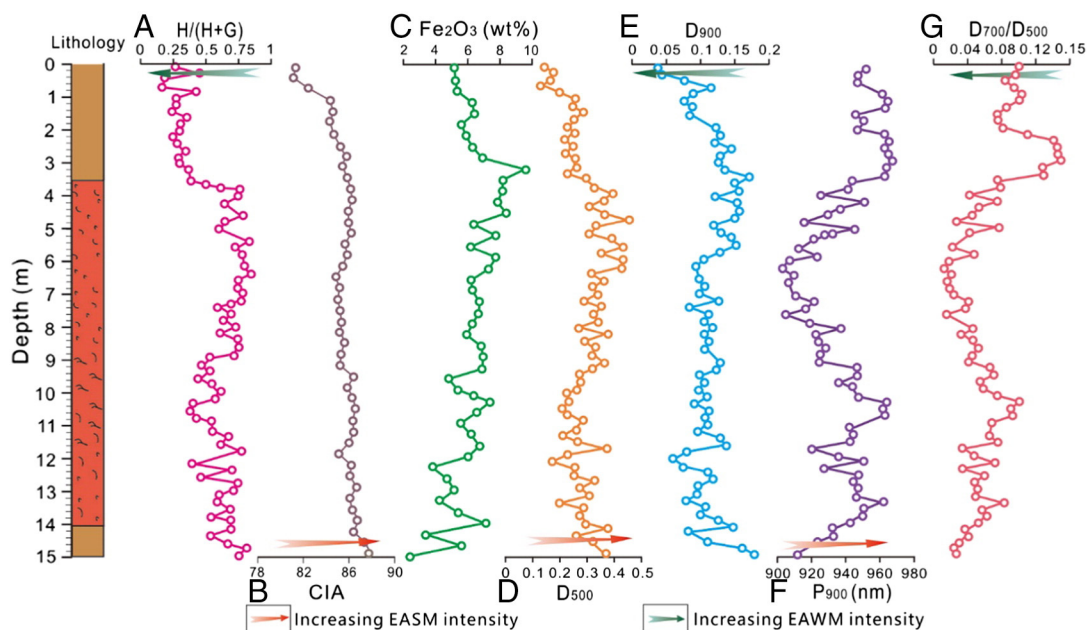


Fig. 5. Profiles of (A) Fe-oxides, (B–C) geochemical data (from Zhao et al., 2017), and (D–G) spectral parameters: (A) $H/(H+G)$, (B) CIA, (C) Fe_2O_3 , (D) D_{500} , (E) D_{900} , (F) P_{900} , and (G) D_{700}/D_{500} .

3A), Al substitution into Fe-oxides causes a ${}^6A_{1g} \rightarrow {}^4T_{1g}$ crystal field transition, resulting in a shift toward longer wavelengths (Cudahy and Ramanaidou, 1997). For example, 33% replacement of Fe^{3+} by Al^{3+} can shift P_{900} by 30 nm (Buckingham and Sommer, 1983). Grain size has no apparent effect on absorption band position in the VNIR range, although a change in grain size from >75 to $<20 \mu m$ shifts P_{900} toward longer wavelengths by 30 nm (Cudahy and Ramanaidou, 1997).

The broad VNIR absorption band from 902 to 963 nm with a nadir at 937 nm (Fig. 4) does not have a simple interpretation, because both the incorporation of aluminum and the presence of other ferric Fe-oxides can shift P_{900} toward longer wavelengths. This band brackets the 915-nm band associated with Al-free goethite but reflects a broadening and a shift toward longer wavelengths, suggesting a mixture of mineral

phases. If the degree of substitution of Al into Fe-oxides is variable within the sample, this could account for both the broadening and the positive shift of the absorption band. A second possibility is the presence of lepidocrocite, which is a common weathering product and has a weak absorption band at ~ 960 nm (Tapert et al., 2011). Therefore, the rightward shift of P_{900} values may have been caused by the incorporation of aluminum and/or the presence of lepidocrocite.

In the study samples, changes in absorption bands in the VNIR region can be interpreted in terms of the presence or concentration of Fe-oxide phases, rather than grain size or elemental (e.g., Al) substitution. VNIR spectral features are largely controlled by Fe-oxide concentrations, as shown by the strong correlation of P_{900} and D_{700}/D_{500} values ($r = +0.96$, $n = 76$, $p < 0.001$). The P_{900} -versus- D_{700}/D_{500}

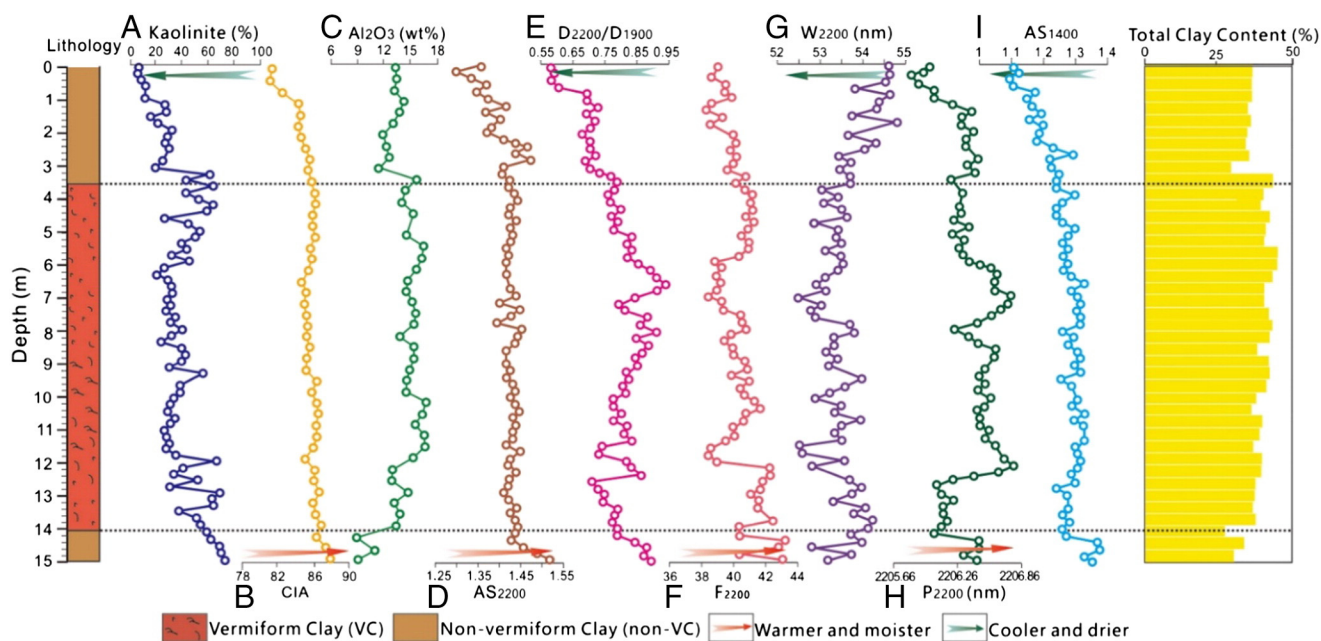


Fig. 6. Profiles of (A) clay minerals, (B–C) geochemical data (from Zhao et al., 2017), and (D–I) spectral parameters: (A) kaolinite, (B) CIA, (C) Al_2O_3 , (D) AS_{2200} , (E) D_{2200}/D_{1900} , (F) F_{2200} , (G) W_{2200} , (H) P_{2200} , and (I) AS_{1400} .

relationship is best fit by a third-order polynomial curve (Fig. 8A), which suggests that specific P_{900} values are associated with extremely high D_{700}/D_{500} ratios ($P_{900} = \sim 960$ nm), reflecting a dominant goethite fraction, and extremely low D_{700}/D_{500} ratios ($P_{900} = \sim 900$ nm), reflecting a dominant hematite fraction.

Concentrations of molecular water and OH (hydroxyl) ions influence the SWIR part of the absorption spectrum, especially the ~ 1400 -nm band. We found excellent correlations between D_{1400} and D_{1900} ($r = +0.94$, $n = 76$; $p < 0.001$; Fig. 8B) and between D_{1400} and D_{2200} ($r = +0.96$, $n = 76$; $p < 0.001$; Fig. 8C). The absorption band at ~ 1900 nm may be influenced not only by hydrous minerals but also by vegetation and surface waters (Doublier et al., 2010a). The high correlation of D_{1400} and D_{1900} indicates that the detected water is mostly bound in the interlayer region of hydrous minerals (Baldridge et al., 2009; Hecker et al., 2011). The absorption band at ~ 2200 nm is mainly influenced by clay minerals (i.e., kaolinite, illite), and the strong correlation of D_{1400} with D_{2200} reflects the presence of molecular water mainly in clay minerals (Doublier et al., 2010b). A single dominant water source makes these spectral features useful indicators for our purposes.

5.2. Utility of VNIR spectral parameters as monsoonal weathering proxies

The mineralogy and abundances of Fe-oxides in a sample can be quantified on the basis of its VNIR spectrum (Fig. 5; Murphy and

Monteiro, 2013). Ferric oxide abundance is strongly related to the intensity of crystal field absorption near 900 nm (Cudahy and Ramanaidou, 1997). In the RESs of the present study, elevated Fe content is recorded by both the ~ 500 nm and ~ 900 nm bands, with the intensity of the latter (D_{900}) serving as the best proxy for ferric iron concentration. In profile, the P_{900} and D_{700}/D_{500} parameters tend to exhibit similar variation trends and an inverse relationship with the $H/(H + G)$ ratio (Fig. 5F–G), yielding a strong negative correlation ($r = -0.81$, $n = 76$; $p < 0.001$; Fig. S1B). At higher $H/(H + G)$ ratios, the ~ 900 -nm band exhibits a shift toward shorter wavelengths.

These findings lay the foundation for use of surface reflectance VNIR spectra in the remote detection of iron ore deposits, which can be a more efficient and less costly approach than field surveys (Rajendran et al., 2011; Ciampalini et al., 2013). Moreover, the strong correlations between spectral parameters and Fe-oxide mineralogy documented in this study demonstrate that it is possible to spectrally assess the grade of iron ores in surface deposits, with larger D_{900} values indicating higher-quality ferric iron ores (Magendran and Sanjeevi, 2014).

Monsoonal intensification can have multiple effects on soil parameters, including grain size distribution, clay-mineral composition, and Fe-oxide mineralogy, as well as the carbon and oxygen isotopes of terrestrial carbonate deposits (Sun et al., 2006; He et al., 2013; Yu et al., 2016; Zhao et al., 2017). These effects result from higher rates of chemical weathering in warmer and more humid environments, which are associated with monsoon intensity (West et al., 2005; Clift et al., 2014).

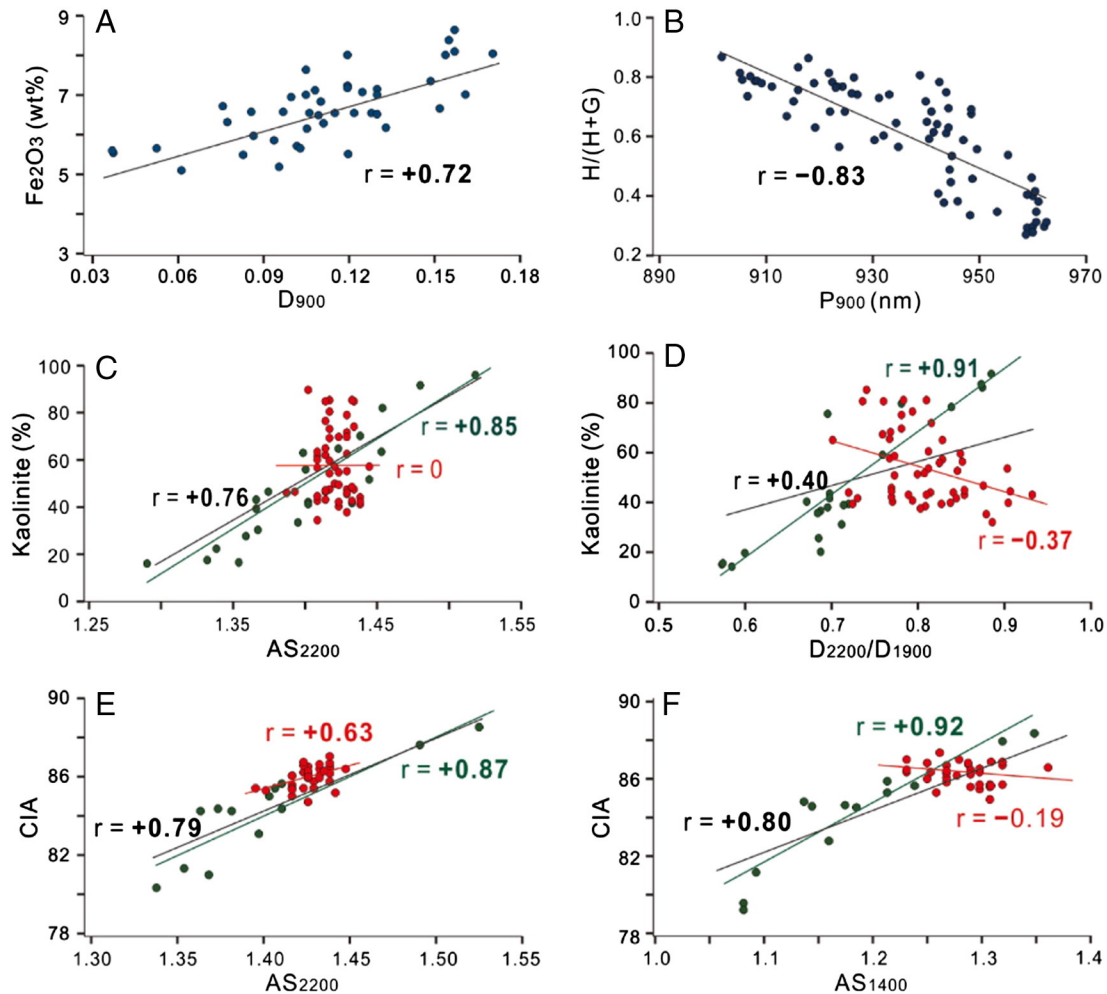


Fig. 7. (A) VSWIR spectral parameters versus percent Fe(III) oxide. (B) Correlation between VSWIR spectral parameters and hematite amount (given as the $H/(H + G)$ ratio). (C–D) VSWIR spectral parameters versus kaolinite amount. (E–F) VSWIR spectral parameters versus CIA. The red dots represent vermiform clay (VC) samples from the silty clay and upper sandy clay units, and the green dots correspond to samples from other parts of the section (non-VC samples). Bold text indicates statistically significant r values ($p < 0.05$).

Hematite concentration is enhanced under alternating wet and dry conditions and warm temperatures (see Section 2.2). Previous research has shown that the $H/(H + G)$ ratio can be applied as a paleomonsoon proxy (Torrent et al., 2007; Zhao et al., 2017), and the strong correlations of $H/(H + G)$ with the P_{900} and D_{700}/D_{500} spectral parameters ($r = -0.83$ and -0.81 , respectively; $n = 76$; $p < 0.001$; Fig. 7B and Fig. S1B) indicate that the latter also can be used as monsoonal weathering proxies. Lower values of P_{900} and D_{700}/D_{500} , reflecting greater hematite content, signal warmer and seasonally drier pedoenvironments and, thus, a more intense summer monsoon (Fig. 5F–G).

5.3. Utility of SWIR spectral parameters as monsoonal weathering proxies

The profiles of SWIR spectral parameters and some geochemical weathering proxies are shown in Fig. 6. The AS_{2200} parameter represents the asymmetry of the Al–OH absorption band and depends only on features of the band itself. This parameter has been found to be useful for assessing mineral alteration in previous studies (Hauff et al., 1991; Fang et al., 2017a). Soils with high illite content yield relatively symmetric bands (i.e., $AS_{2200} \sim 1$), whereas those with high kaolinite content yield asymmetric bands (i.e., $AS_{2200} > 1$, or leftward asymmetry) (Bendor et al., 2003). The strong correlations of AS_{2200} with kaolinite and CIA ($r = +0.76$ and $+0.79$, respectively; $n = 76$; $p < 0.001$; Fig. 7C, E) indicate that variations in the shape and symmetry of the Al–OH band reflect weathering intensity. AS_{2200} values can change slightly depending on substitutions of Al, Fe, or Mg into the mineral lattice (Bendor and Banin, 1994). Similar to AS_{2200} , AS_{1400} also exhibits a strong correlation to CIA values ($r = +0.80$; $n = 46$; $p < 0.001$; Fig. 7F). The AS_{1400} parameter is related to overtones of molecular water and hydroxyl, and its increase reflects a transition to warmer and wetter conditions. The D_{2200}/D_{1900} parameter is affected by changes in molecular water content and the degree of mineral alteration (Doublier et al., 2010b).

An interesting finding is that the exclusion of the VC samples leads to greatly improved correlations of SWIR spectral parameters with clay minerals and CIA values (Fig. 8 and Fig. S1). The relationships between the spectral parameters used in the present study (e.g., D_{2200}/D_{1900} , AS_{2200} , AS_{1400}) and clay-mineral/geochemical data are all excellent for the non-VC samples alone, with values of $|r|$ ranging from 0.83 to 0.99 ($n = 12$ or 24 ; $p < 0.001$; Fig. 7 and Fig. S1). However, correlations for the VC samples alone are weak to non-existent, with $|r|$ ranging from 0 to 0.66, reflecting limitations on the use of spectral properties for weathering intensity estimates. A likely cause of the poor correlations of spectral parameters with clay-mineral/geochemical weathering proxies for the VC samples is their pronounced compositional heterogeneity. This heterogeneity is due to intense localized Fe leaching influenced by microorganisms and groundwater table fluctuations, and may affect the crystal structure of the clay minerals. The nature of the “OH” bands (including OH, H_2O , and AIOH bands) differ in the white veins/spots versus red matrix, introducing variance in the spectral data. For this reason, weathering intensity is best predicted using the spectral parameters of the non-VC samples. For these samples, variation in weathering intensity is strongly positively correlated to AS_{2200} , D_{2200}/D_{1900} , F_{2200} , P_{2200} and AS_{1400} and inversely correlated to W_{2200} (Fig. 6).

5.4. Implications for paleoclimate reconstruction and imaging spectroscopy (IS)

Various spectral parameters discussed above have been shown to be good weathering proxies, among which three groups can be distinguished. The first group is based on ferric iron absorption features centered at ~ 500 , ~ 700 , and ~ 900 nm. The spectral parameters in this group (i.e., P_{900} and D_{700}/D_{500}) are highly correlated with hematite amount, showing excellent potential as paleomonsoon climate proxies. In particular, higher P_{900} and D_{700}/D_{500} values indicate weakening of the summer monsoon. The second group of parameters is based on OH and/or H_2O absorption features at either ~ 1400 nm or ~ 1900 nm. The best

correlation is shown by the AS_{1400} versus CIA ($r = +0.80$). The third group is based only on the 2200 nm feature (i.e., AIOH band). The correlations observed for this group are slightly better than for the second group with best values of $r = +0.76$ (AS_{2200} versus kaolinite) and $r = +0.79$ (AS_{2200} versus CIA). The changes in peak shape measured by these parameters are due to an increase of crystal lattice ordering and, possibly, increasing homogenization of metal–(OH)–metal bond angles (Doublier et al., 2010b). The parameters of the second and third groups (i.e., AS_{2200} , AS_{1400} and D_{2200}/D_{1900}) are thus good proxies for weathering and paleoclimate reconstruction.

The utility of the investigated spectral proxies depends mainly on the mineral composition of soils and the application type (i.e., laboratory versus field; Fig. 9). The first group is suitable for various soil types, and it is more advantageous when the soils is inhomogeneous (e.g., those having vermiform structure). The second group, which integrates changes in water and hydroxyl content, may be problematic if vegetation and surface water are present, such as in swamps and hydromorphic soils (Cudahy et al., 2016; Hong et al., 2016). For laboratory studies, the peak correction procedure as outlined in OH and H_2O correction results can be useful. The third group is based only on the AIOH band and therefore lacks influence by water and hydroxyl ions. For relative homogeneous soils, the spectral parameters of the AIOH band are robust for climate reconstruction. This group is strongly influenced by kaolinite-group minerals, and it is particularly suited for field studies because it is not influenced by vegetation and surface water (Doublier et al., 2010b).

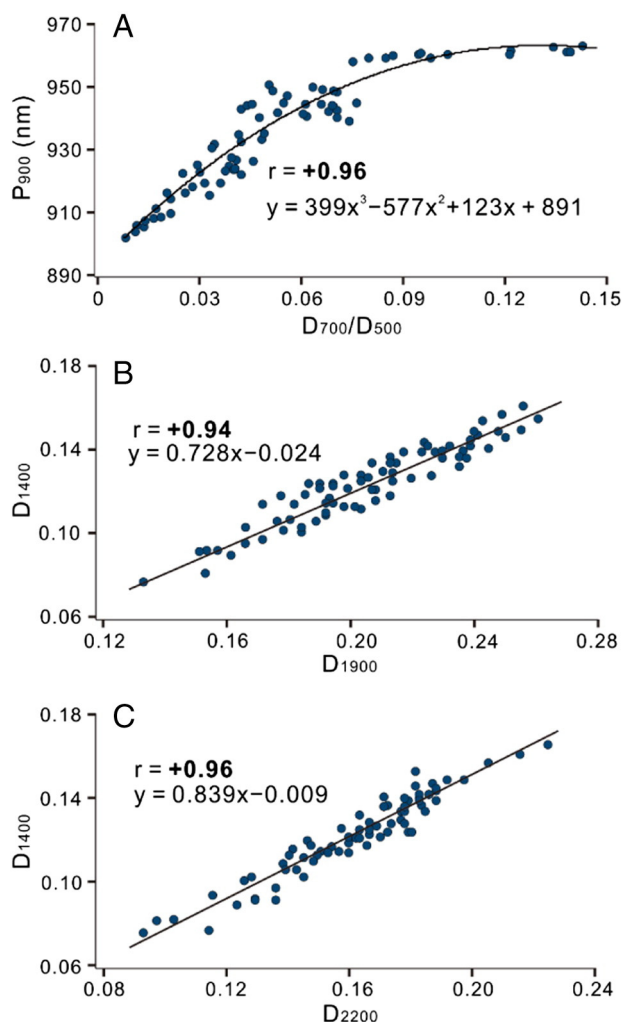


Fig. 8. (A) P_{900} versus D_{700}/D_{500} , (B) D_{1400} versus D_{1900} , and (C) D_{1400} versus D_{2200} . Bold text indicates statistically significant r values ($p < 0.001$).

In the present work, we demonstrate the utility of VSWIR spectroscopy for estimating the clay content, molecular water content, and weathering intensity of soils. One promising application of VSWIR spectroscopy is for field-based studies, e.g., the imaging spectroscopy (IS) technique, which is also known as hyperspectral remote sensing. IS can exploit information carried by absorption bands in the VSWIR range, and it is a useful technique to remotely identify and map soil properties (Goetz et al., 1985; Bendor et al., 2008; Kruse, 2012; Lyu et al., 2017). It brings a new dimension to the field of remote sensing by enlarging the envelope of point spectrometry into a spatial domain. Most commonly, data are acquired from airborne or space-borne platforms, and the potential of those imaging spectrometers has long been applied to monitor Earth's surface and to provide valuable information for better understanding many environmental features and processes related to vegetation, ecology, soils, coastal and inland waters, snow properties, and archaeological exploration (Sims and Gamon, 2003; Ustin et al., 2004; Schaepman et al., 2009; van der Meer et al., 2012; Moses et al., 2012). Recent advances in scanning technology have enabled data to be acquired from sensors mounted on field-based platforms (Kurz et al., 2011; Murphy and Monteiro, 2013; Cudahy et al., 2016). Earlier studies have characterized soil mineralogy and geochemistry for climatic information, but they were generally local surveys over relatively small areas and/or did not contain spatial referencing data. The ability of IS to remotely monitor spectral features of soil surfaces, especially in relatively isolated and inaccessible regions, provides an opportunity for regional investigations of weathering intensity and paleoclimate variation.

6. Conclusions

Red earth sediments from the Shengli section, Sichuan Basin were investigated using a rapid and effective VSWIR spectroscopic approach. Spectral features in the VNIR range are best interpreted in terms of the presence and concentration of individual Fe-oxide phases, rather than in terms of grain size or elemental substitutions in mineral lattices. The detected water is mostly bound in clay minerals, and this single dominant water source facilitates interpretation of SWIR spectral

parameters. Iron content in the red earth sediments can be distinguished by absorption bands at both ~500 nm and ~900 nm, although the latter is a distinctly better proxy for ferric iron concentration. Lower intensities of the P_{900} and D_{700}/D_{500} proxies indicate warmer and seasonally drier pedoenvironments as well as greater summer monsoon intensity.

The utility of SWIR spectral parameters as weathering intensity changes depending on the homogeneity of soil. These spectral parameters are effective in relative homogeneous soils, but some of them lose their ability to accurately predict clay mineral content and composition and, thus, weathering intensity in the VC samples. In general, weathering intensity is therefore better estimated using the spectral parameters of non-VC samples, for which greater weathering intensity is highly correlated to AS_{2200} , D_{2200}/D_{1900} , and AS_{1400} . The utility of these spectral proxies depends mainly on the mineral composition of soils and the application type (i.e., laboratory versus field). The parameters based on absorption features at ~1400 nm and ~1900 nm may be problematic in field areas in which vegetation and shallow groundwater/surface water are present. The spectral parameters based on the ~2200 nm absorption band are influenced strongly by kaolinite-group minerals, especially when the soil is relative homogeneous. The application of VSWIR in the field (e.g., imaging spectroscopy, or IS) shows promise, providing an opportunity for rapid mapping of weathering intensity over larger areas, especially in relatively remote and inaccessible regions.

Supplementary data to this article can be found online at <http://dx.doi.org/10.1016/j.palaeo.2017.07.007>.

Acknowledgments

This study was supported by the Natural Science Foundation of China (41472041, 41272053 and U1602232), the NSFC for Young Scholars (41402036 and 41602037), NSF of Hubei for Young Scholars (2016CFB183), Postdoctoral Science Foundation of China (2015M582301). TJA acknowledges support from the NASA Exobiology program (NNX13AJ1IG) and the China University of Geosciences-Wuhan (SKL-GPMR 201301 and SKL-BGEG BGL21407). LZ acknowledges

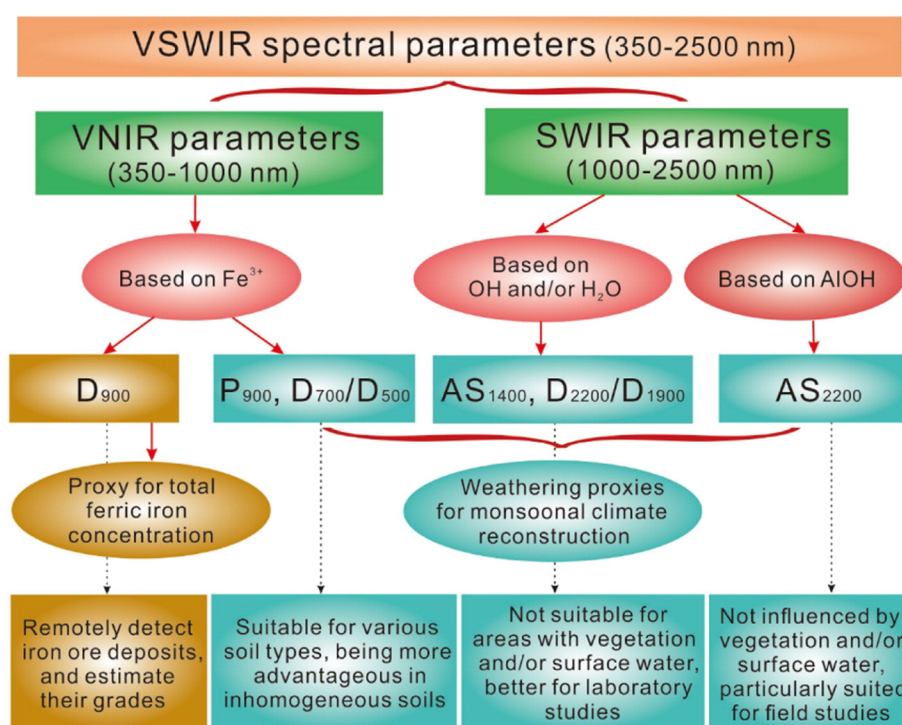


Fig. 9. Summary figure of applications and limitations of various spectral parameters.

the China Scholarship Council (CSC) for financial support (201706410006). We are grateful to Rongbiao Li and Wenli Zhang for assistance in the field and Fei Hu, Yeqing Liu, Bing Xu, Zhuang Duan, Hongqiang Wang, Xi Chen and Cheng Fang for help with laboratory work.

References

- Adeline, K.R.M., Gomez, C., Gorretta, N., Roger, J.M., 2017. Predictive ability of soil properties to spectral degradation from laboratory Vis-NIR spectroscopy data. *Geoderma* 288, 143–153.
- Algeo, T.J., Hannigan, R., Rowe, H., Brookfield, M., Baud, A., Krystyn, L., Ellwood, B.B., 2007. Sequencing events across the Permian-Triassic boundary, Guryul Ravine (Kashmir, India). *Palaeogeogr. Palaeoclimatol. Palaeoecol.* 252, 328–346.
- An, Z.S., 2000. The history and variability of the East Asian paleomonsoon climate. *Quat. Sci. Rev.* 19, 171–187.
- Anderson, S.P., Blum, J., Brantley, S.L., Chadwick, O., Chorover, J., Derry, L.A., Drever, J.I., Hering, J.G., Kirchner, J.W., Kump, L.R., 2004. Proposed initiative would study Earth's weathering engine. *Eos Trans. Am. Geophys. Union* 85, 265–269.
- Anderson, S.P., von Blanckenburg, F., White, A.F., 2007. Physical and chemical controls on the critical zone. *Elements* 3, 315–319.
- Baldrige, A.M., Hook, S.J., Grove, C.I., Rivera, G., 2009. The ASTER spectral library version 2.0. *Remote Sens. Environ.* 113, 711–715.
- Banfield, J.F., Barker, W.W., Welch, S.A., Taunton, A., 1999. Biological impact on mineral dissolution: application of the lichen model to understanding mineral weathering in the rhizosphere. *Proc. Natl. Acad. Sci. U. S. A.* 96, 3404–3411.
- Ben-Dor, E., Banin, A., 1994. Visible and near-infrared (0.4–1.1 μm) analysis of arid and semiarid soils. *Remote Sens. Environ.* 48, 261–274.
- Bendor, E., Goldshleger, N., Benyamini, Y., Agassi, M., Blumberg, D.G., 2003. The spectral reflectance properties of soil structural crusts in the 1.2- to 2.5- μm spectral region. *Soil Sci. Soc. Am. J.* 67, 289–299.
- Bendor, E., Taylor, R.G., Hill, J., Dematté, J.A.M., Whiting, M.L., Chabrilat, S., Sommer, S., 2008. Imaging spectrometry for soil applications. *Adv. Agron.* 97, 321–392.
- Bo, S., Rossel, R.A.V., Mouazen, A.M., Wetterlind, J., 2010. Chapter five—visible and near-infrared spectroscopy in soil science. *Adv. Agron.* 107, 163–215.
- Brady, N.C., Weil, R.R., 2000. *Elements of the Nature and Properties of Soils*. Prentice Hall, Upper Saddle River, New Jersey (738 pp).
- Brantley, S.L., Goldhaber, M.B., Ragnarsdottir, K.V., 2007. Crossing disciplines and scales to understand the critical zone. *Elements* 3, 307–314.
- Buckingham, W.F., Sommer, S.E., 1983. Mineralogical characterization of rock surfaces formed by hydrothermal alteration and weathering-application to remote sensing. *Econ. Geol.* 78, 664–674.
- Buggle, B., Glaser, B., Hambach, U., Gerasimenko, N., Marković, S., 2011. An evaluation of geochemical weathering indices in loess-paleosol studies. *Quat. Int.* 240, 12–21.
- Buggle, B., Hambach, U., Mueller, K., Zoeller, L., Markovic, S.B., Glaser, B., 2014. Iron mineralogical proxies and quaternary climate change in SE-European loess-paleosol sequences. *Catena* 117, 4–22.
- Burns, R.G., 1993. *Mineralogical Applications of Crystal Field Theory*. 2nd ed. Cambridge Univ. Press, Cambridge (551 pp).
- Ceryan, S., Tudes, S., Ceryan, N., 2008. A new quantitative weathering classification for igneous rocks. *Environ. Geol.* 55, 1319–1336.
- Chamley, H., 1989. Clay formation through weathering. In: Chamley, H. (Ed.), *Clay Sedimentology*. Springer, Berlin, pp. 21–50.
- Chen, J., An, Z., Head, J., 1999. Variation of Rb/Sr ratios in the loess-paleosol sequences of central China during the last 130,000 years and their implications for monsoon paleoclimatology. *Quat. Res.* 51, 215–219.
- Chen, T., Xie, Q., Xu, H., Chen, J., Ji, J., Lu, H., Balsam, W., 2010. Characteristics and formation mechanism of pedogenic hematite in Quaternary Chinese loess and paleosols. *Catena* 81, 217–225.
- Chorover, J., Kretzschmar, R., Garcia-Pichel, F., Sparks, D.L., 2007. Soil biogeochemical processes within the critical zone. *Elements* 3, 321–326.
- Ciampalini, A., Garfagnoli, F., Del Ventisette, C., Moretti, S., 2013. Potential use of remote sensing techniques for exploration of iron deposits in western Sahara and southwest of Algeria. *Nat. Resour. Res.* 22, 179–190.
- Clark, R.N., 1999. Spectroscopy of rocks and minerals and principles of spectroscopy. In: Rencz, A.N. (Ed.), *Remote Sensing for the Earth Sciences*. Wiley, Chichester, pp. 3–58.
- Clark, R.N., Roush, T.L., 1984. Reflectance spectroscopy: quantitative analysis techniques for remote sensing applications. *J. Geophys. Res.* 89, 6329–6340.
- Clark, R.N., King, T., Klejwa, M., Swayze, G.A., Vergo, N., 1990. High spectral resolution reflectance spectroscopy of minerals. *J. Geophys. Res.—Solid Earth* 95, 12653–12680.
- Clark, R.N., Swayze, G.A., Wise, R., Livo, K.E., Hoefen, T.M., Kokaly, R.F., Sutley, S.J., 2007. USGS digital spectral library splib06a. U.S. Geological Survey, Digital Data Series 231.
- Clift, P.D., Wan, S., Blusztajn, J., 2014. Reconstructing chemical weathering, physical erosion and monsoon intensity since 25 Ma in the northern South China Sea: a review of competing proxies. *Earth Sci. Rev.* 130, 86–102.
- Cornell, R.M., Schwertmann, U., 2003. *The Iron Oxides: Structure, Properties, Reactions, Occurrences and Uses*. 2nd ed. Wiley-VCH Verlag, Weinheim, Germany, pp. 703–712.
- Cudahy, T.J., Ramanaidou, E.R., 1997. Measurement of the hematite: goethite ratio using field visible and near-infrared reflectance spectrometry in channel iron deposits, western Australia. *Aust. J. Earth Sci.* 44, 411–420.
- Cudahy, T., Caccetta, M., Thomas, M., Hewson, R., Abrams, M., Kato, M., Kashimura, O., Ninomiya, Y., Yamaguchi, Y., Collings, S., Laukamp, C., Ong, C., Lau, I., Rodger, A., Chia, J., Warren, P., Woodcock, R., Fraser, R., Rankine, P., Vote, J., de Caritat, P., English, P., Meyer, D., Doescher, C., Fu, B., Shi, P., Mitchell, R., 2016. Satellite-derived mineral mapping and monitoring of weathering, deposition and erosion. *Sci Rep* 6, 1–12.
- Cullers, R.L., 2000. The geochemistry of shales, siltstones and sandstones of Pennsylvanian-Permian age, Colorado, USA: implications for provenance and metamorphic studies. *Lithos* 51, 181–203.
- Da Cruz, R.S., Dias Fernandes, C.M., Nobre Villas, R.N., Juliani, C., Soares Monteiro, L.V., Ribeiro De Almeida, T.I., Lagler, B., Carneiro, C.D.C., Echeverri Misas, C.M., 2015. A study of the hydrothermal alteration in Paleoproterozoic volcanic centers, Sao Felix do Xingu region, Amazonian Craton, Brazil, using short-wave infrared spectroscopy. *J. Volcanol. Geotherm. Res.* 304, 324–335.
- Dasch, E.J., 1969. Strontium isotopes in weathering profiles, deep-sea sediments, and sedimentary rocks. *Geochim. Cosmochim. Acta* 33, 1521–1552.
- Deng, C.L., Zhu, R.X., Verosub, K.L., Singer, M.J., Vidic, N.J., 2004. Mineral magnetic properties of loess/paleosol couplets of the central loess plateau of China over the last 1.2 Myr. *J. Geophys. Res.—Solid Earth* 109, 241–262.
- Dettman, D.L., Fang, X., Garzione, C.N., Li, J., 2003. Uplift-driven climate change at 12 Ma: a long $\delta^{18}\text{O}$ record from the NE margin of the Tibetan plateau. *Earth Planet. Sci. Lett.* 214, 267–277.
- Dixon, J.L., Chadwick, O.A., Vitousek, P.M., 2016. Climate-driven thresholds for chemical weathering in postglacial soils of New Zealand. *J. Geophys. Res.—Earth Surf.* 121, 1619–1634.
- Doublier, M.P., Roache, T., Potel, S., 2010a. Short-wavelength infrared spectroscopy: a new petrological tool in low-grade to very low-grade pelites. *Geology* 38, 1031–1034.
- Doublier, M.P., Roache, A., Potel, S., 2010b. Application of SWIR spectroscopy in very low-grade metamorphic environments: a comparison with XRD methods. *Geol. Surv. West. Aust. Rec. (Manual)* (61 pp).
- Dufrechou, G., Grandjean, G., Bourguignon, A., 2015. Geometrical analysis of laboratory soil spectra in the short-wave infrared domain. Clay composition and estimation of the swelling potential. *Geoderma* 243, 92–107.
- Duke, E.F., 1994. Near infrared spectra of muscovite, Tschermak substitution, and metamorphic reaction progress: implications for remote sensing. *Geology* 22, 621–624.
- Eberl, D.D., Smith, D.B., 2009. Mineralogy of soils from two continental-scale transects across the United States and Canada and its relation to soil geochemistry and climate. *Appl. Geochem.* 24, 1394–1404.
- Fang, Q., Churchman, G.J., Hong, H., Chen, Z.Q., Liu, J., Yu, J., Han, W., Wang, C., Zhao, L., Furnes, H., 2017a. New insights into microbial smectite illitization in the Permo-Triassic boundary K-bentonites, South China. *Appl. Clay Sci.* 140, 96–111.
- Fang, Q., Hong, H., Zhao, L., Furnes, H., Lu, H., Han, W., Liu, Y., Jia, Z., Wang, C., Yin, K., Algeo, T.J., 2017b. Tectonic uplift-influenced monsoonal changes promoted hominin occupation of the Luonan Basin: insights from a loess-paleosol sequence, eastern Qinling Mountains, central China. *Quat. Sci. Rev.* 169, 312–329.
- Farmer, V.C., Russell, J.D., 1964. The infra-red spectra of layer silicates. *Spectrochim. Acta* 20, 1149–1173.
- Fedo, C.M., Nesbitt, H.W., Young, G.M., 1995. Unraveling the effects of potassium metasomatism in sedimentary rocks and paleosols, with implications for paleoweathering conditions and provenance. *Geology* 23, 921–924.
- Gaffey, S.J., McFadden, L.A., Nash, D., Pieters, C.M., 1993. Ultraviolet, visible, and near-infrared reflectance spectroscopy: laboratory spectra of geologic materials. In: Pieters, C.M., Englert, P.E. (Eds.), *Remote Geochemical Analysis: Elemental and Mineralogical Composition*. Topics in Remote Sensing Series Vol. 4. Cambridge University Press, Cambridge, United Kingdom, pp. 43–77.
- Gislason, S.R., Oelkers, E.H., Eiriksdottir, E.S., Kardjilov, M.I., Gisladdottir, G., Sigfusson, B., Snorrason, A., Elfsen, S., Hardardottir, J., Torssander, P., 2009. Direct evidence of the feedback between climate and weathering. *Earth Planet. Sci. Lett.* 277, 213–222.
- Goetz, A.F.H., Vane, G., Solomon, J.E., Rock, B.N., 1985. Imaging spectrometry for Earth remote sensing. *Science* 228, 1147–1153.
- Gong, H., Zhang, R., Yue, L., Zhang, Y., Li, J., 2015. Magnetic fabric from red clay sediments in the Chinese Loess Plateau. *Sci Rep* 5, 9701–9706.
- Han, J.M., Keppens, E., Liu, T.S., Paepe, R., Jiang, W.Y., 1997. Stable isotope composition of the carbonate concretion in loess and climate change. *Quat. Int.* 37, 37–43.
- Han, W., Fang, X., Yang, S., King, J., 2010. Differences between East Asian and Indian monsoon climate records during MIS3 attributed to differences in their driving mechanisms: evidence from the loess record in the Sichuan basin, southwestern China and other continental and marine climate records. *Quat. Int.* 218, 94–103.
- Haufl, P.L., Kruse, F.A., Madrid, R.J., Fraser, S., Huntington, J., Jones, M., Watters, S., 1991. Illite crystallinity—case histories using X-ray diffraction and reflectance spectroscopy to define ore host environments. Proceedings of the 8th Thematic Conference on Geological Remote Sensing, May 2, 1991, pp. 447–458 Boulder, Colorado.
- He, T., Chen, Y., Balsam, W., Qiang, X., Liu, L., Chen, J., Ji, J., 2013. Carbonate leaching processes in the red clay formation, Chinese Loess Plateau: fingerprinting East Asian summer monsoon variability during the late Miocene and Pliocene. *Geophys. Res. Lett.* 40, 194–198.
- Hecker, C., Hook, S., Meijde, M.V.D., Bakker, W., Werff, H.V.D., Wilbrink, H., Ruitenbeek, F.V., Smeth, B.D., Meer, F.V.D., 2011. Thermal infrared spectrometer for Earth-science remote sensing applications—instrument modifications and measurement procedures. *Sensors* 11, 10981–10999.
- Hong, H., Gu, Y., Yin, K., Zhang, K., Li, Z., 2010. Red soils with white net-like veins and their climate significance in South China. *Geoderma* 160, 197–207.
- Hong, H., Gu, Y., Yin, K., Wang, C., Li, Z., 2013. Clay record of climate change since the mid-Pleistocene in Jiujiang, South China. *Boreas* 42, 173–183.
- Hong, H., Fang, Q., Cheng, L., Wang, C., Churchman, G.J., 2016. Microorganism-induced weathering of clay minerals in a hydromorphic soil. *Geochim. Cosmochim. Acta* 184, 272–288.
- Hošek, J., Hambach, U., Lisá, L., Grygar, T.M., Horáček, I., Meszner, S., Kněšl, I., 2015. An integrated rock-magnetic and geochemical approach to loess/paleosol sequences from Bohemia and Moravia (Czech Republic): implications for the Upper Pleistocene

- paleoenvironment in central Europe. *Palaeogeogr. Palaeoclimatol. Palaeoecol.* 418, 344–358.
- Hu, X., Wei, J., Xu, L., Zhang, G., Zhang, W., 2009. Magnetic susceptibility of the Quaternary red clay in subtropical China and its paleoenvironmental implications. *Palaeogeogr. Palaeoclimatol. Palaeoecol.* 279, 216–232.
- Hu, X., Wei, J., Du, Y., Xu, L., Wang, H., Zhang, G., Ye, W., Zhu, L., 2010. Regional distribution of the Quaternary red clay with aeolian dust characteristics in subtropical China and its paleoclimatic implications. *Geoderma* 159, 317–334.
- Hu, P., Liu, Q., Heslop, D., Roberts, A.P., Jin, C., 2015. Soil moisture balance and magnetic enhancement in loess-paleosol sequences from the Tibetan Plateau and Chinese Loess Plateau. *Earth Planet. Sci. Lett.* 409, 120–132.
- Huang, C., Zhao, W., Liu, F., Tan, W., Koopal, L.K., 2011. Environmental significance of mineral weathering and pedogenesis of loess on the southernmost Loess Plateau, China. *Geoderma* 163, 219–226.
- Hyun, C.U., Park, H.D., 2011. Assessment of chemical weathering of granite stone monuments using reflectance spectroscopy. *Bull. Eng. Geol. Environ.* 70, 63–78.
- Islam, K., Singh, B., McBratney, A., 2003. Simultaneous estimation of several soil properties by ultra-violet, visible, and near-infrared reflectance spectroscopy. *Aust. J. Soil Res.* 41, 1101–1114.
- Jahn, B., Gallet, S., Han, J., 2001. Geochemistry of the Xining, Xifeng and Jixian sections, loess plateau of China: eolian dust provenance and paleosol evolution during the last 140 ka. *Chem. Geol.* 178, 71–94.
- Jeong, G.Y., Hillier, S., Kemp, R.A., 2011. Changes in mineralogy of loess-paleosol sections across the Chinese Loess Plateau. *Quat. Res.* 75, 245–255.
- Kruse, F.A., 2012. Mapping surface mineralogy using imaging spectrometry. *Geomorphology* 137, 41–56.
- Kurz, T.H., Buckley, S.J., Howell, J.A., Schneider, D., 2011. Integration of panoramic hyperspectral imaging with terrestrial lidar data. *Photogramm. Rec.* 26, 212–228.
- Lee, C.T., Morton, D.M., Little, M.G., Kistler, R., Horodyskyj, U.N., Leeman, W.P., Agranier, A., 2008. Regulating continent growth and composition by chemical weathering. *Proc. Natl. Acad. Sci. U. S. A.* 105, 4981–4986.
- Li, Y., Song, Y., Chen, X., Li, J., Mamadjanov, Y., Aminov, J., 2016. Geochemical composition of Tajikistan loess and its provenance implications. *Palaeogeogr. Palaeoclimatol. Palaeoecol.* 446, 186–194.
- Liu, Z., Colin, C., Li, X., Zhao, Y., Tuo, S., Chen, Z., Siringan, F.P., Liu, J.T., Huang, C., You, C., Huang, K., 2010. Clay mineral distribution in surface sediments of the northeastern South China Sea and surrounding fluvial drainage basins: source and transport. *Mar. Geol.* 277, 48–60.
- Lu, S., Wang, S., Chen, Y., 2015. Palaeopedogenesis of red palaeosols in Yunnan Plateau, southwestern China: pedogenical, geochemical and mineralogical evidences and palaeoenvironmental implication. *Palaeogeogr. Palaeoclimatol. Palaeoecol.* 420, 35–48.
- Lü, X., Versteegh, G.J.M., Song, J., Li, X., Yuan, H., Li, N., 2016. Geochemistry of Middle Holocene sediments from South Yellow Sea: implications to provenance and climate change. *J. Earth Sci.* 27, 751–762.
- Lyu, C., Cheng, Q., Zuo, R., Wang, X., 2017. Mapping spatial distribution characteristics of lineaments extracted from remote sensing image using fractal and multifractal models. *J. Earth Sci.* 28, 507–515.
- Magendran, T., Sanjeevi, S., 2014. Hyperion image analysis and linear spectral unmixing to evaluate the grades of iron ores in parts of Noamundi, eastern India. *Int. J. Appl. Earth Obs. Geoinf.* 26, 413–426.
- Maher, B.A., 1998. Magnetic properties of modern soils and Quaternary loessic paleosols: paleoclimatic implications. *Palaeogeogr. Palaeoclimatol. Palaeoecol.* 137, 25–54.
- McLennan, S.M., 1993. Weathering and global denudation. *J. Geol.* 101, 295–303.
- van der Meer, F.D., 2004. Analysis of spectral absorption features in hyperspectral imagery. *Int. J. Appl. Earth Obs. Geoinf.* 5, 55–68.
- van der Meer, F.D., van der Werff, H.M., van Ruitenbeek, F.J., Hecker, C.A., Bakker, W.H., Noomen, M.F., van der Meijde, M., Carranza, E.J.M., de Smeth, J.B., Woldai, T., 2012. Multi- and hyperspectral geologic remote sensing: a review. *Int. J. Appl. Earth Obs. Geoinf.* 14, 112–128.
- Mohanty, B., Gupta, A., Das, B.S., 2016. Estimation of weathering indices using spectral reflectance over visible to mid-infrared region. *Geoderma* 266, 111–119.
- Moses, W.J., Gitelson, A.A., Perk, R.L., Gurlin, D., Rundquist, D.C., Leavitt, B.C., Barrow, T.M., Brakhage, P., 2012. Estimation of chlorophyll-a concentration in turbid productive waters using airborne hyperspectral data. *Water Res.* 46, 993–1004.
- Mulder, V.L., Plötze, M., de Bruin, S., Schaepman, M.E., Mavris, C., Kokaly, R.F., Egli, M., 2013. Quantifying mineral abundances of complex mixtures by coupling spectral deconvolution of SWIR spectra (2.1–2.4 μm) and regression tree analysis. *Geoderma* 207–208, 279–290.
- Murphy, R.J., Monteiro, S.T., 2013. Mapping the distribution of ferric iron minerals on a vertical mine face using derivative analysis of hyperspectral imagery (430–970 nm). *ISPRS J. Photogramm. Remote Sens.* 75, 29–39.
- Murphy, R.J., Schneider, S., Monteiro, S.T., 2014. Consistency of measurements of wavelength position from hyperspectral imagery: use of the ferric iron crystal field absorption at ~ 900 nm as an indicator of mineralogy. *IEEE Trans. Geosci. Remote Sens.* 52, 2843–2857.
- Nesbitt, H.W., Young, G.M., 1982. Early Proterozoic climates and plate motions inferred from major element chemistry of lutites. *Nature* 299, 715–717.
- Nesbitt, H.W., Fedo, C.M., Young, G.M., 1997. Quartz and feldspar stability, steady and non-steady-state weathering, and petrogenesis of siliciclastic sands and muds. *J. Geol.* 105, 173–192.
- Nocita, M., Stevens, A., van Wesemael, B., Brown, D.J., Shepherd, K.D., Towett, E., Vargas, R., Montanarella, L., 2015. Soil spectroscopy: an opportunity to be seized. *Glob. Chang. Biol.* 21, 10–11.
- Oh, H., Shin, H.J., 2016. Climatic classification over Asia during the middle holocene climatic optimum based on PMIP models. *J. Earth Sci.* 27, 123–129.
- Price, J.R., Velbel, M.A., 2003. Chemical weathering indices applied to weathering profiles developed on heterogeneous felsic metamorphic parent rocks. *Chem. Geol.* 202, 397–416.
- Rajendran, S., Thirunavukkarasu, A., Balamurugan, G., Shankar, K., 2011. Discrimination of iron ore deposits of granulite terrain of Southern Peninsular India using ASTER data. *J. Asian Earth Sci.* 41, 99–106.
- Rosolen, V., Lamotte, M., Boulet, R., Trichet, J., Rouer, O., Melfi, A.J., 2002. Genesis of a mottled horizon by Fe-depletion within a laterite cover in the Amazon basin. *Compt. Rendus Geosci.* 334, 187–195.
- Schaepman, M.E., Ustin, S.L., Plaza, A.J., Painter, T.H., Verrelst, J., Liang, S., 2009. Earth system science related imaging spectroscopy—an assessment. *Remote Sens. Environ.* 113, 123–137.
- Shaw, J.N., Hajek, B.F., Beck, J.M., 2010. Highly weathered mineralogy of select soils from southeastern US coastal plain and piedmont landscapes. *Geoderma* 154, 447–456.
- Sheldon, N.D., Tabor, N.J., 2009. Quantitative paleoenvironmental and paleoclimatic reconstruction using paleosols. *Earth Sci. Rev.* 95, 1–52.
- Sheldon, N.D., Retallack, G.J., Tanaka, S., 2002. Geochemical climofunctions from North American soils and application to paleosols across the Eocene-Oligocene boundary in Oregon. *J. Geol.* 110, 687–696.
- Sheng, X., Chen, J., Ji, J., Chen, T., Li, G., H., H., 2008. Morphological characters and multi-element isotopic signatures of carbonates from Chinese loess-paleosol sequences. *Geochim. Cosmochim. Acta* 72, 4323–4337.
- Sims, D.A., Gamon, J.A., 2003. Estimation of vegetation water content and photosynthetic tissue area from spectral reflectance: a comparison of indices based on liquid water and chlorophyll absorption features. *Remote Sens. Environ.* 84, 526–537.
- Soriano-Disla, J.M., Janik, L.J., Rossel, R.A.V., Macdonald, L.M., McLaughlin, M.J., 2014. The performance of visible, near-, and mid-infrared reflectance spectroscopy for prediction of soil physical, chemical, and biological properties. *Appl. Spectrosc. Rev.* 49, 139–186.
- Stockmann, U., Minasny, B., McBratney, A.B., 2011. Quantifying processes of pedogenesis. *Adv. Agron.* 113, 1–71.
- Summers, D., Lewis, M., Ostendorf, B., Chittleborough, D., 2011. Visible near-infrared reflectance spectroscopy as a predictive indicator of soil properties. *Ecol. Indic.* 11, 123–131.
- Sun, Y., Lu, H., An, Z., 2006. Grain size of loess, palaeosol and red clay deposits on the Chinese Loess Plateau: significance for understanding pedogenic alteration and palaeomonsoon evolution. *Palaeogeogr. Palaeoclimatol. Palaeoecol.* 241, 129–138.
- Sun, Z., Owens, P.R., Han, C., Chen, H., Wang, X., Wang, Q., 2016. A quantitative reconstruction of a loess-paleosol sequence focused on paleosol genesis: an example from a section at Chaoyang, China. *Geoderma* 266, 25–39.
- Tappert, M., Rivard, B., Giles, D., Tappert, R., Mauger, A., 2011. Automated drill core logging using visible and near-infrared reflectance spectroscopy. *Econ. Geol.* 106, 289–296.
- Terhorst, B., Ottner, F., Wriessnig, K., 2012. Weathering intensity and pedostratigraphy of the Middle to Upper Pleistocene loess/paleosol sequence of Wels-Aschet (Upper Austria). *Quat. Int.* 265, 142–154.
- Thiry, M., 2000. Palaeoclimatic interpretation of clay minerals in marine deposits: an outlook from the continental origin. *Earth Sci. Rev.* 49, 201–221.
- Timothy, A.G., James, M.R., John, F.M., James, W.H., 2017. A 40,000 yr record of clay mineralogy at Lake Towuti, Indonesia: paleoclimate reconstruction from reflectance spectroscopy and perspectives on paleolakes on Mars. *Geol. Soc. Am. Bull.* 129, 806–819.
- Torrent, J., Liu, Q., Bloemendal, J., Barron, V., 2007. Magnetic enhancement and iron oxides in the upper Luochuan loess-paleosol sequence, Chinese Loess Plateau. *Soil Sci. Soc. Am. J.* 71, 1570–1578.
- Townsend, T.E., 1987. Discrimination of iron alteration minerals in visible and near-infrared reflectance data. *J. Geophys. Res.—Solid Earth* 92, 1441–1454.
- Újvári, G., Varga, A., Raucsik, B., Kovács, J., 2014. The Paks loess-paleosol sequence: a record of chemical weathering and provenance for the last 800 ka in the mid-Carpathian Basin. *Quat. Int.* 319, 22–37.
- Ustin, S.L., Roberts, D.A., Gamon, J.A., Asner, G.P., Green, R.O., 2004. Using imaging spectroscopy to study ecosystem processes and properties. *Bioscience* 54, 523–534.
- Varga, A., Újvári, G., Raucsik, B., 2011. Tectonic versus climatic control on the evolution of a loess-paleosol sequence at Beremend, Hungary: an integrated approach based on paleoecological, clay mineralogical, and geochemical data. *Quat. Int.* 240, 71–86.
- Viscarra Rossel, R.A., 2011. Fine-resolution multiscale mapping of clay minerals in Australian soils measured with near infrared spectra. *J. Geophys. Res.—Earth Surf.* 116, 1–15.
- Viscarra Rossel, R.A., Walvoort, D.J.J., McBratney, A.B., Janik, L.J., Skjemstad, J.O., 2006. Visible, near infrared, mid infrared or combined diffuse reflectance spectroscopy for simultaneous assessment of various soil properties. *Geoderma* 131, 59–75.
- Viscarra Rossel, R.A., Behrens, T., Ben-Dor, E., Brown, D.J., Demattê, J.A.M., Shepherd, K.D., Shi, Z., Stenberg, B., Stevens, A., Adamchuk, V., Aichi, H., Barthès, B.G., Bartholomeus, H.M., Bayer, A.D., Bernoux, M., Böttcher, K., Brodsky, L., Du, C.W., Chappell, A., Fouad, Y., Genot, V., Gomez, C., Grunwald, S., Gubler, A., Guerrero, C., Hedley, C.B., Knadel, M., Morrás, H.J.M., Nocita, M., Ramirez-Lopez, L., Roudier, P., Campos, E.M.R., Sanborn, P., Sellitto, V.M., Sudduth, K.A., Rawlins, B.G., Walter, C., Winowiecki, L.A., Hong, S.Y., Ji, W., 2016. A global spectral library to characterize the world's soil. *Earth-Sci. Rev.* 155, 198–230.
- Wan, S., Toucanne, S., Clift, P.D., Zhao, D., Bayon, G., Yu, Z., Cai, G., Yin, X., Revillon, S., Wang, D., Li, A., Li, T., 2015. Human impact overwhelms long-term climate control of weathering and erosion in southwest China. *Geology* 43, 439–442.
- Wang, Q., Yang, S., 2013. Clay mineralogy indicates the Holocene monsoon climate in the Changjiang (Yangtze River) catchment, China. *Appl. Clay Sci.* 74, 28–36.
- Wang, S., Lin, S., Lu, S., 2013. Rock magnetism, iron oxide mineralogy and geochemistry of Quaternary red earth in central China and their paleopedogenic implication. *Palaeogeogr. Palaeoclimatol. Palaeoecol.* 379–380, 95–103.

- West, A., Galy, A., Bickle, M., 2005. Tectonic and climatic controls on silicate weathering. *Earth Planet. Sci. Lett.* 235, 211–228.
- White, A., 2008. Quantitative approaches to characterizing natural chemical weathering rates. In: Brantley, S., Kubicki, J., White, A.F. (Eds.), *Kinetics of Water–Rock Interaction*. Springer, New York, pp. 469–500.
- Wilson, M.J., 2004. Weathering of the primary rock-forming minerals: processes, products and rates. *Clay Miner.* 39, 233–266.
- Xiong, S., Ding, Z., Zhu, Y., Zhou, R., Lu, H., 2010. A ~6 Ma chemical weathering history, the grain size dependence of chemical weathering intensity, and its implications for provenance change of the Chinese loess–red clay deposit. *Quat. Sci. Rev.* 29, 1911–1922.
- Yang, S., Fang, X., Shi, Z., Lehmkuhl, F., Song, C., Han, Y., Han, W., 2010. Timing and provenance of loess in the Sichuan Basin, southwestern China. *Palaeogeogr. Palaeoclimatol. Palaeoecol.* 292, 144–154.
- Yu, Z., Wan, S., Colin, C., Yan, H., Bonneau, L., Liu, Z., Song, L., Sun, H., Xu, Z., Jiang, X., 2016. Co-evolution of monsoonal precipitation in East Asia and the tropical Pacific ENSO system since 2.36 Ma: new insights from high-resolution clay mineral records in the West Philippine Sea. *Earth Planet. Sci. Lett.* 446, 45–55.
- Zhang, W., Yu, L., Lu, M., Zheng, X., Ji, J., Zhou, L., Wang, X., 2009. East Asian summer monsoon intensity inferred from iron oxide mineralogy in the Xiashu Loess in southern China. *Quat. Sci. Rev.* 28, 345–353.
- Zhao, L., Hong, H., Fang, Q., Yin, K., Wang, C., Li, Z., Torrent, J., Cheng, F., Algeo, T.J., 2017. Monsoonal climate evolution in southern China since 1.2 Ma: new constraints from Fe-oxide records in red earth sediments from the Shengli section, Chengdu Basin. *Palaeogeogr. Palaeoclimatol. Palaeoecol.* 473, 1–15.
- Zheng, G., Jiao, C., Zhou, S., Shang, G., 2016. Analysis of soil chronosequence studies using reflectance spectroscopy. *Int. J. Remote Sens.* 37, 1881–1901.